Field Simulation for the Microwave Heating of Thin Ceramic Fibers

by

Nathaniel D. Terril

Thesis submitted to the Faculty of the

Virginia Polytechnic Institute and State University

in partial fulfillment of the requirements for the degree of

MASTER OF SCIENCE

in

Electrical Engineering

Dr. W. A. Davis, Chairman
Dr. J. R. Thomas
Dr. A. Safaai-Jazi

9 July 1998
Blacksburg, Virginia

Key Words: Ceramics, Microwave, Field, Heating, Thermal Runaway

Field Simulation for the Microwave Heating of Thin Ceramic Fibers

by

Nathaniel Dale Terril

Dr. W. A. Davis, Chairman

Electrical Engineering

(ABSTRACT)

Microwave processing of ceramics has seen a growth in research and development efforts throughout the past decade. One area of interest is the exploration of improved heating control through experiments and numerical modeling. Controlled heating may be used to counteract non-uniform heating and avoid destructive phenomena such as cracking and thermal runaway. Thermal runaway is a potential problem in materials with temperature dependent dielectric properties. As the material absorbs electromagnetic energy, the temperature increases as does its ability to absorb more energy. Controlled processing of the material may be achieved by manipulating the applied field. The purpose of this research is to model the interaction of the EM-field with a thin ceramic fiber to investigate possible mechanisms that may affect the heating process. The fiber undergoes microwave heating in a single-mode resonant applicator. Maxwell's equations for the fields within the cavity are solved using mode-matching techniques taking into account the field interaction of the fiber and an arbitrarily shaped coupling aperture. Effects of varying the aperture shape on the field distribution are explored. The coupled nature of the electromagnetic solution with the material's temperature-dependent properties, including an analysis of non-uniform heating, is also discussed.

Acknowledgments

I would like to express my gratitude to my advisor Dr. William A. Davis for all of his time and patience over the past year and a half. His ability to explain a problem from various points of view helped me understand concepts I found difficult to comprehend. Dr. Davis spent many hours outside of class instructing me in the electromagnetics area. I am very grateful for his support.

I also would like to thank Dr. James R. Thomas, professor in mechanical engineering at Virginia Tech, for educating me on the experiments in microwave processing performed at Los Alamos National Laboratory.

I would like to thank Dr. Ahmad Safaai-Jazi and Dr. Thomas for their time and for being on my advisory committee.

Finally I thank my family and friends for their support during my time at Virginia Tech. The love and encouragement from my parents helped me greatly. In particular I want to thank my girlfriend Deandra who supported me always and endured my sometimes difficult work habits.

Table of Contents

Chapter Title

1 INTRODUCTION....1
1.1 Background....1
1.2 Literature Review....2
1.3 Thesis Overview....6

2 PRESENTATION OF THE PROBLEM....7
2.1 Past and Current Experiments....7
2.2 The Electromagnetic Cavity Problem....8
2.3 General Field Solution Formulation Using Mode-Matching Techniques....9
2.3.1 Basic Equations....9
2.3.2 Waveguide Boundary Conditions and Resultant Modes....13
2.3.3 Mode-matching Concepts....19
2.3.4 Method of Moments Solution....22
2.3.5 Aperture Interface....23
2.3.6 Fiber Interface....29
2.4 Thermal Solution Considerations....34
2.4.1 Material Properties....35

3 APPLICATION OF SOLUTION....37
3.1 Aperture Solution....37
3.1.1 Basis and Weighting Functions....39
3.1.2 Verification....41
3.2 Fiber Solution....44
3.2.1 Verification....44
3.2.2 Non-uniform Heating....46
3.3 Complete Field Solution....48
3.3.1 Modified Aperture Solution....48
3.3.2 Modified Fiber Solution....50
3.3.3 Combined Fiber and Aperture Problems....53
3.3.4 Field Distribution Results....54
3.3.5 Restricted Mode Solution....63

4 CONCLUSION....64
4.1 Summary....64
4.2 Conclusion....65
4.3 Recommendations....66

REFERENCES....67

VITA....69

List of Figures

FIGURE 1.1 Flowchart for Microwave Heating Analysis..... 3

FIGURE 2.1 Diagram of Problem Statement..... 8

FIGURE 2.2 Solution Regions..... 11

FIGURE 2.3 Axial Behavior of Transverse Fields..... 13

FIGURE 2.4 Geometry for Aperture Mode-Matching..... 20

FIGURE 2.5 Aperture Interface..... 24

FIGURE 2.6 Fiber Interface..... 29

FIGURE 2.7*a* Dielectric Constant of Mullite vs. Temperature..... 35

FIGURE 2.7*b* Dielectric Loss of Mullite vs. Temperature..... 36

FIGURE 3.1a Comparison of Computed and Tabulated Aperture Reactance..... 42

FIGURE 3.1b Comparison of Computed and Tabulated Aperture Susceptance..... 42

FIGURE 3.2 Convergence of Green's Function and Magnetic Current..... 43

FIGURE 3.3a Comparison of Computed and Tabulated Real Reflection Coefficient..... 45

FIGURE 3.3b Comparison of Computed and Tabulated Imaginary Reflection Coefficient..... 46

FIGURE 3.4 Fiber Interface Including Short..... 50

FIGURE 3.5 E_y Distribution in Cavity for the $y = b$ Plane..... 54

FIGURE 3.6 Peak Electric Field Increase at Fiber vs. Dielectric Constant and Fiber Diameter..... 55

FIGURE 3.7 Cavity Detuning Effects for Various Fibers..... 56

FIGURE 3.8 Electric Field Strength vs. Temperature for 20W Constant Absorbed Power for a 2mm Ceramic Rod..... 57

FIGURE 3.9 Comparison of Electric Field vs. Temperature Relationships for Electromagnetic and Thermal Results..... 58

FIGURE 3.10*a* Temperature Distribution for Stationary Heating..... 59

FIGURE 3.10*b* Relative Permittivity of Fiber for Non-Uniform Stationary Heating..... 59

FIGURE 3.10*c* Electric Field Profile Along Fiber for Stationary Heating..... 60

FIGURE 3.11*a* Temperature Distribution for Continuous Heating..... 61

FIGURE 3.11*b* Relative Permittivity of Fiber for Non-Uniform Continuous Heating..... 61

FIGURE 3.11*c* Electric Field Profile Along Fiber for Continuous Heating..... 62

FIGURE 3.12 E_y Distribution in Cavity for the $x = a/2$ Plane..... 63

1. Introduction

1.1 Background

Microwave processing of materials offers a number of advantages over conventional heating methods. Microwave energy can penetrate the material, achieving rapid internal heating which may also improve the structural properties of the product. Along with the possibility of more controlled heating, this results in an efficient process that has the potential to reduce the requirements on time and energy. Applications include sintering, drying, and joining. Although still in a developmental stage, there has been an increase in research and development efforts throughout the last decade. Much of the research is directed at overcoming the challenges of microwave processing through modeling and experiments with the long term goal of developing microwave processing for industrial applications [1].

One particular problem with microwave heating of interest to this research is thermal runaway. Many materials processed by microwaves, including the ceramic fibers or rods discussed in this paper, are characterized by dielectric properties that increase strongly with temperature. The temperature of a material depends on the electric field strength along the material and the material's dielectric loss. As the material absorbs energy, its temperature increases with a corresponding relatively large increase in the dielectric loss. The higher loss allows the material to absorb more energy resulting in a higher temperature. If the power absorbed is left unchecked, thermal runaway may occur as the material quickly heats until it breaks down.

The research presented in this thesis is related to the research by past graduate students Wilfried Duchez [2] and Craig Goodson [3] completed in 1996 and 1997, respectively. Working under Dr. James R. Thomas, Jr. at Virginia Tech, they investigated the microwave heating of ceramic fibers and rods based on experiments performed at the Los Alamos National Laboratory (LANL). Duchez developed a one-dimensional finite difference model to explore the conditions necessary to achieve stable, high temperature heating of zirconia and alumina fibers. His model also accounted for continuous processing by allowing the fiber to move through the cavity at a set velocity. He

demonstrated that a desired temperature distribution along a fiber could be obtained by specifying the profile of the electric field strength along the fiber. The desired temperature distribution was such that the fiber reached stable temperatures high enough for sintering without going into thermal runaway.

The research performed by Goodson extended the thermal model to two dimensions allowing for temperature variations along the radius of the fiber. The two-dimensional model was required to accurately model thicker fibers and rods. He found that by varying the electric field strength to hold the power absorbed by the fiber constant, thermal runaway problems could be avoided. This is a more accurate representation of the experiment since the power source provides a constant power, not necessarily a constant field strength at the fiber. Goodson also obtained temperature distribution profiles along the fiber which showed the formation of a hot spot near the midpoint of the fiber. He also showed the migration of the hot spot during continuous processing which was consistent with experimental results observed at LANL.

1.2 Literature Review

The potential benefits of microwave processing, as well as the problems encountered, have stimulated many researchers to investigate numerical modeling techniques to gain a better understanding of how microwaves interact with materials. To accurately model microwave heating, both electromagnetic and heat transfer equations must be solved. A flowchart [4] depicting the procedure for a typical microwave heating analysis is shown in Fig. 1.1. In addition, the two separate analyses are coupled through the temperature-dependent dielectric properties of the load. The dielectric loss, or the measure of the material's ability to absorb energy, increases rapidly with temperature in certain materials. This effect is attributed to the fact that interstitial atoms become free at high temperatures and absorption is greater in the free state than in the bound state [5]. An overview of various approaches to analyzing microwave heating of ceramics is presented in this section.

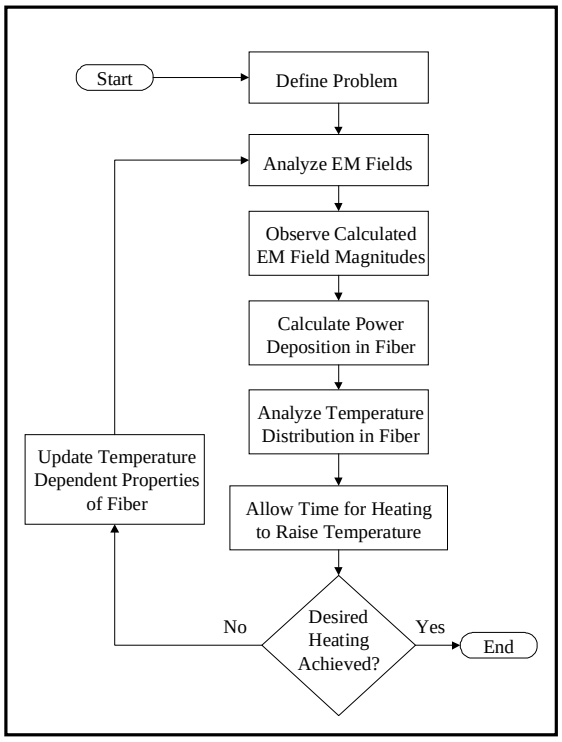

Fig. 1.1 Flowchart for Microwave Heating Analysis

The finite-difference time-domain (FDTD) method is the most common method used to solve the differential equations governing the heat transfer problem. This method has also been employed extensively by Iskander et al. [4,6,7] in solving the coupled electromagnetic field and heat transfer equations. Iskander has investigated the use of both single and multi-mode cavities for microwave sintering through FDTD simulations. For larger samples, multi-mode cavities appear to generate a more uniform temperature distribution [6]. A single-mode FDTD simulation was also developed which accounts for the effects of the sample size and electrical parameters on the resonant frequency of the cavity and the corresponding heating patterns [7]. The simulation results show quantitatively the resonant frequency shifts of a given cavity for variations in the dielectric constant of the material and the size of the coupling iris. The detuning effects could be significant since tuning may be limited to a finite range in industrial applications.

Another method used to analyze the electromagnetic field interaction with a ceramic sample is the finite element method (FEM). Dibben et al. [8] used edge elements to discretize the system in three dimensions. They demonstrated that this method compared well to results obtained using a finite-difference method. To couple the EM solution to the heat transfer equations, they suggested an iterative procedure. The heat transfer equations are solved in the time-domain using the EM field results computed for the temperature in the previous step. The new temperature obtained from the heat transfer solution would then be used to find a new set of permittivity parameters and hence solve for the new EM field. The process is repeated until the temperature converges.

A similar iterative procedure is described by Clemens et al. [9]. They iteratively coupled separate FDTD solutions to the electromagnetic and heat transfer equations. Since the time for the thermal response is much longer than that of the electromagnetic response, the EM solution may be used to update the heat transfer solution when necessary. This is determined from a set criterion based on the temperature-dependent dielectric properties of the material.

One problem observed in the microwave heating of ceramic fibers is the formation of hot spots in the sample. These hot spots, from which thermal runaway may occur, have been reported to develop after relatively small increases in power [10]. Kriegsmann [11] developed a mathematical heat transfer model to investigate the formation of hot spots. By including the cavity detuning effects resulting from the change in the dielectric loss of the sample as the temperature increased, he showed that localized regions of high temperature formed as a result of thermal perturbations. In addition, he found that the peak temperature and size of the hot spot were dependent on the thickness of the fiber. The peak temperature decreased and the hot spot became more diffuse as the radius of the fiber increased.

Another approach presented by Hile et al. [12] is a hybrid electromagnetic solution. They applied scattering matrix theory using asymptotic field formulations to describe interactions of the coupling iris, ceramic material, and short. This analysis assumes that the material is far enough away from the iris and short that evanescent modes excited by the iris and the material do not interact with the each other or the short. A

numerical method is then used to solve for the fields in the waveguide containing the ceramic, not including the iris. After the reflection coefficient for the fiber and short are obtained, the iris is incorporated through the scattering matrix equations. Although the FDTD method was chosen in this analysis to solve for the fields, the specific numerical method is not limited to FDTD.

Physical implementation of controlled microwave heating was demonstrated by Vogt et al. [13] by controlling power and frequency of a traveling wave tube amplifier. A feedback control system adjusted the frequency to maintain resonance and monitored power output to hold the amount of power absorbed constant. This approach is somewhat limited to experimental heating. Implementation on a large scale, such as an industrial process, could be difficult since many industrial microwave applicators do not allow for variable frequencies [3].

In summary, one of the major topics of research is the analysis of hot spot formation and the resulting effects on the heating process. Several approaches have been taken to simulate microwave heating of ceramics including FDTD, FEM, and hybrid methods. The FDTD method has the capability of solving the coupled heat transfer and EM equations dynamically in the time-domain. An alternative to this approach is to update the heat transfer solution with the EM solution as necessary to achieve a dynamic model. This is possible because of the large disparity in the time scale of the thermal and EM transients. In this case, the EM analysis is not limited to the FDTD method. Rather, the choice is open to other solutions such as the finite element method or an asymptotic method. The analysis of hot spots in microwave heating simulations is important since the dielectric properties have a strong dependence on temperature. An uncontrolled hot spot can quickly enter thermal runaway in which the material is destroyed. This research accounts for hot spot formations by including temperature-dependent properties in the EM solution. The relative permittivity of the fiber is modeled as a function of position to allow for a temperature distribution along the fiber.

1.3 Thesis Overview

The objective of this research is to develop a simulation of the electromagnetic fields inside a cavity during the microwave heating of a ceramic fiber. The model is based on the experiments performed at LANL used in the research by Duchez [2] and Goodson [3]. We will explore any potential variations in the profile of the electric field strength along the fiber caused by shaping the coupling aperture. This solution will also provide a method for resolving the coupled nature of the thermal and electromagnetic solutions. The temperature-dependent dielectric properties of the fiber are incorporated into the field solution. This allows us to explore thermal coupling effects such as the variations in the field strength and absorbed power as the temperature of the fiber changes. In addition, a non-constant temperature distribution along the fiber may be simulated by modeling the fiber as an inhomogeneous material based on its temperature-dependent dielectric properties.

The electromagnetic field solution to the problem at hand is developed in several parts. First, the basic equations and solution techniques are presented to familiarize the reader with the notation and methods used throughout the analysis. We then construct the field solution to the aperture and fiber interfaces individually as sub-components of the complete problem. These solutions are then combined to obtain a set of matrix equations which are implemented in a computer program to generate results to the full problem.

2. Presentation of the Problem

2.0 Chapter Overview

The microwave heating problem under consideration in this thesis is based on experiments performed at the Los Alamos National Laboratory (LANL) [14]. The purpose of this chapter is to develop the fundamental concepts necessary to solve for the electromagnetic fields in the microwave heating simulation. An overview of the experimental setup is presented which outlines the physical parameters to be modeled. In addition, the basic equations required to formulate the solution are introduced. Finally, the impact of material properties on the field solution as well as the thermal coupling is discussed.

2.1 Past and Current Experiments

Recent experiments at LANL [14] investigated the single-mode microwave heating of thin ceramic fibers and rods. The experiment involved inserting a ceramic fiber vertically through two holes in the top and bottom of a water cooled copper WR284 waveguide. A coupling aperture and an adjustable short were placed in the waveguide creating a cavity between them with the fiber located at an approximate resonant peak. The aperture coupled energy into the cavity from a broad band traveling wave tube amplifier operating at 2.93 GHz. Continuous processing of the fiber was investigated by using a stepping motor to feed the fiber through the cavity at a constant velocity. Experimental data included temperature of the sample, input and reflected power, and remote video of the heating process.

The experiments investigated the heating of mullite rods ranging in diameter from 1mm to 5mm. The temperature and power data were taken at one second intervals. The input power and frequency were adjusted to obtain stable temperatures during both continuous and stationary processing. As the fiber absorbed energy, a hot spot formed near its midpoint. The hot spot quickly entered thermal runaway when the absorption of power was uncontrolled. A heat transfer analysis of the heating process showed that the

hot spot forms predominately as a result of axial heat conduction toward the ends of the fiber [3].

2.2 The Electromagnetic Cavity Problem

The research presented here provides a method of solution for obtaining the electromagnetic fields within the cavity including the field interaction effects of the coupling aperture, the short, and the fiber. The solution is implemented in a computer program to obtain numerical results.

The solution of the electric field distribution along the fiber requires resolving the interaction of the incident field with the aperture, fiber, and cavity properties. Figure 2.1 shows the model of the experimental setup at Los Alamos used for this analysis. The mathematical model consists of a modal expansion of $TE^{(z)}$ and $TM^{(z)}$ modes satisfying the boundary conditions of the waveguide and cavity walls. Boundary conditions are also applied at the aperture and fiber interfaces to determine the complete solution. The fiber is ultimately modeled as an inhomogeneous dielectric rod.

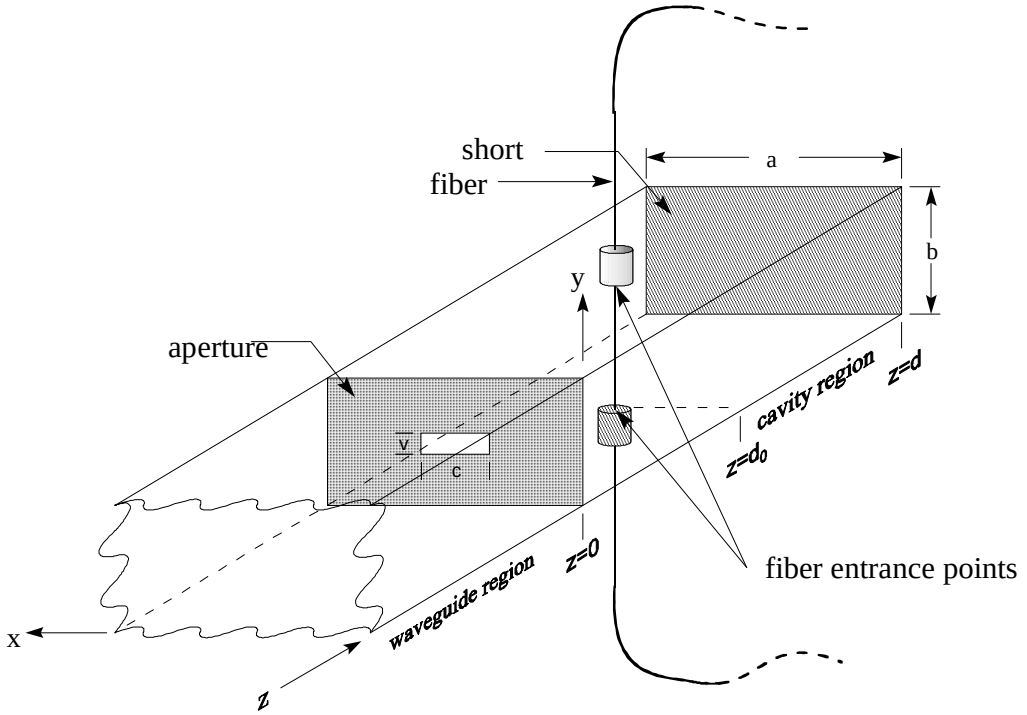

Fig. 2.1 Diagram of Problem Statement

The waveguide walls, aperture, and shorting plane are assumed to be perfect electric conductors when applying boundary conditions. A perturbational technique is used to include loss in the longitudinal walls of the waveguide and cavity as a complex propagation constant of propagating modes. The fiber is assumed to be a cylindrical dielectric rod with a sufficiently small cross-section that the tangential electric fields are continuous throughout the fiber to a good approximation. To include scattering from the fiber, the rod is treated as a line source with current proportional to the equivalent volume current density and the cross-sectional area of the fiber. This equivalent line source is used to relate the fields at the fiber interface. The fields are determined at the aperture interface using a mode-matching approach to formulate a Green's function. The electric field in the aperture is expressed as an independent set of truncated aperture modes found from a series Green's function formulation. These aperture modes are matched to the cavity and incident modes in the vicinity of the aperture.

2.3 Field Solution Formulation Using Mode-Matching Techniques

The problem under consideration involves solving for the field interaction at the aperture, fiber, and shorting plane. Before solving the complete problem, we will first find a form of solution for the fields and develop the basic equations and methods, including mode-matching concepts and the method of moments, for obtaining solutions to the individual problems.

2.3.1 Basic Equations

The source-free Maxwell curl relations in simple media, expressed in vector differential form in terms of the electric and magnetic fields as

$$\begin{aligned} \nabla \times \vec{E} &= -j\omega\mu\vec{H} \\ \nabla \times \vec{H} &= j\omega\epsilon E, \end{aligned} \tag{2.3.1}$$

govern the electromagnetic behavior throughout the region of interest [15]. Auxiliary potential functions are commonly used to uncouple the equations into two separate polarization modes. The transverse-electric mode (TE) or H-mode fields are derived from the electric vector potential $\vec{F}$. The transverse-magnetic mode (TM) or E-mode

fields are derived from the magnetic vector potential $\vec{A}$. The TE and TM-mode polarizations imply fields defined as transverse to a specific direction. In this analysis, the guide is orientated such that propagation is in the z-direction and the transverse coordinates consist of the x-y plane. Therefore, TE and TM-modes are defined as transverse to the z-direction, with a corresponding H_z or E_z field component, respectively.

The time-harmonic electric and magnetic field vectors for a single mode are found directly from the potential functions as

$$\begin{aligned} \vec{E}^h &= -\nabla \times \vec{F} \\ \vec{H}^h &= \frac{1}{j\omega\mu}\left[k^2\vec{F} + \nabla\nabla\cdot\vec{F}\right] \end{aligned} \tag{2.3.2a}$$

$$\begin{aligned} \vec{E}^e &= \frac{1}{j\omega\epsilon}\left[k^2\vec{A} + \nabla\nabla\cdot\vec{A}\right] \\ \vec{H}^e &= \nabla \times \vec{A}, \end{aligned} \tag{2.3.2b}$$

where the superscripts h and e denote fields derived from a TE and TM-mode, respectively, and $\vec{F}$ and $\vec{A}$ are both z-directed. It should be noted that the above equations have not included the permittivity and permeability factors commonly used in the vector potential curl equations. In our application, we shall assume the material properties are piecewise constant. The equations given above are defined according to Harrington's development [16]. The vector potential functions must also satisfy the homogeneous vector Helmholtz equations

$$\begin{aligned} \left(\nabla^2 + k^2\right)\vec{F} &= 0 \\ \left(\nabla^2 + k^2\right)\vec{A} &= 0. \end{aligned} \tag{2.3.3}$$

The rectangular geometry of the problem lends itself to a solution in Cartesian coordinates where Maxwell's equations can be expressed as a set of six coupled scalar partial differential equations. It is possible to either solve these equations directly or first solve for the potential functions. Since the desired fields are transverse to a single direction, the vector potential functions need only to have a single component in the same

direction to uniquely specify the solution. This simplifies the problem to that of solving a scalar Helmholtz equation.

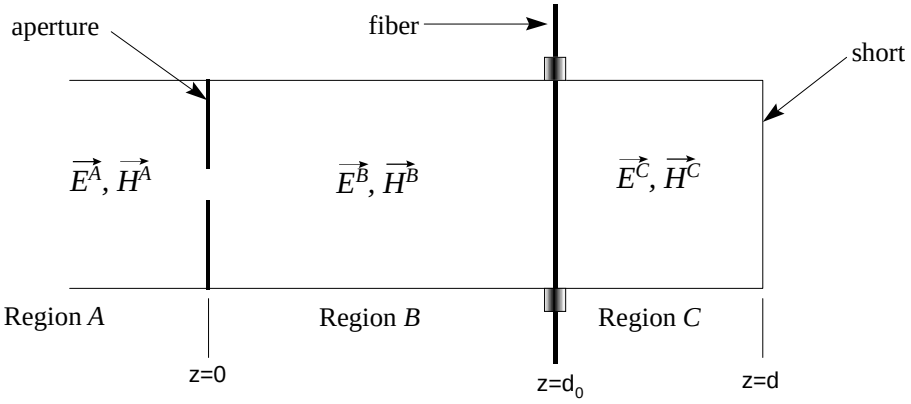

Fig. 2.2 Solution Regions

Since the solution region is longitudinally uniform, it useful to describe the vector potential functions as a product of two scalar functions. One scalar function depends only on transverse position and the other depends only on axial position. Using this approach leads to a straightforward solution to the fields in terms of the specific transverse and axial behavior of the potential functions. For the analysis, the model is divided into three solution regions, as depicted in Fig. 2.2, depending on the longitudinal behavior appropriate to each. This behavior is determined by the nature of the transverse boundaries that terminate each region. In short, the portion of $\vec{F}$ and $\vec{A}$ defined by the transverse scalar functions is the same in each region, while the axial scalar functions defining $\vec{F}$ and $\vec{A}$ are unique to each region. In general, the vector potential functions are defined for each mode as

$$\begin{aligned} \vec{F} &= \hat{z}\psi^h(\vec{\rho})\phi^h(k_z z) \\ \vec{A} &= \hat{z}\psi^e(\vec{\rho})\phi^e(k_z z), \end{aligned} \tag{2.3.4}$$

where $\vec{\rho}$ is the transverse coordinate variable, z is the axial coordinate variable, and k_z is the mode propagation constant. We will assume that the z-dependent scalar function is a harmonic function of $k_z z$ such that

$$\frac{d^2\phi}{dz^2} = -k_z^2\phi, \qquad k_z \text{ real.} \tag{2.3.5}$$

Upon substituting (2.3.4) into (2.3.3), we find that the transverse scalar potential functions ψ^h and ψ^e satisfy the two-dimensional scalar Helmholtz equation

$$\left(\nabla_t^2 + k_c^2\right)\psi = 0, \tag{2.3.6}$$

where

$$k_c^2 = k^2 - k_z^2. \tag{2.3.7}$$

and ∇_t^2 is the transverse portion of the ∇^2 operator. The solution to (2.3.6) is an infinite set of eigenfunctions subject to boundary conditions on the resultant electric field at the longitudinal waveguide walls. The resulting modes in a waveguide are derived from eigenfunction solutions. Each mode has a corresponding discrete value for k_c^2 from which the mode propagation constant is found using (2.3.7) [17].

The mode fields written in terms of the scalar potential functions are

$$\begin{aligned} E_z &= \frac{k_c^2}{j\omega\epsilon}\psi^e\left(\vec{\rho}\right)\phi^e\left(z\right) \\ H_z &= \frac{k_c^2}{j\omega\mu}\psi^h\left(\vec{\rho}\right)\phi^h\left(z\right) \end{aligned} \tag{2.3.8a}$$

$$\boxed{\begin{aligned} \vec{E}_t &= \frac{1}{j\omega\epsilon}\frac{d\phi^e\left(z\right)}{dz}\nabla_t\psi^e\left(\vec{\rho}\right) + \phi^h\left(z\right)\hat{z}\times\nabla_t\psi^h\left(\vec{\rho}\right) \\ \vec{H}_t &= \frac{1}{j\omega\mu}\frac{d\phi^h\left(z\right)}{dz}\nabla_t\psi^h\left(\vec{\rho}\right) - \phi^e\left(z\right)\hat{z}\times\nabla_t\psi^e\left(\vec{\rho}\right), \end{aligned}} \tag{2.3.8b}$$

where the subscripts z and t denote the longitudinal and transverse field components, respectively, and ∇_t is the transverse portion of the ∇ operator. The total fields are a superposition of all such mode fields in the waveguide. The transverse components have been shown separately in (2.3.8) because they are the main focus throughout this paper. The transverse fields provide sufficient information to apply the boundary conditions necessary to solve the problem. The longitudinal field components are not required in the problem at hand.

Each of the three solution regions defined for this analysis can be classified as one of two types: waveguide or cavity. Figure 2.3 shows the types of regions and the axial field behavior associated with each. A typical waveguide region contains fields described

as modes traveling in either the forward or backward direction down the waveguide. The fields in a cavity region are described as standing waves created by the transverse shorting plane placed in the waveguide. We will first develop a solution form for the fields in each region, expressed as a superposition of modes, with each mode having an unknown amplitude. Once these solution forms are obtained, we can compute the unknown mode amplitudes in terms of the incident field by applying boundary conditions at the interfaces between the regions.

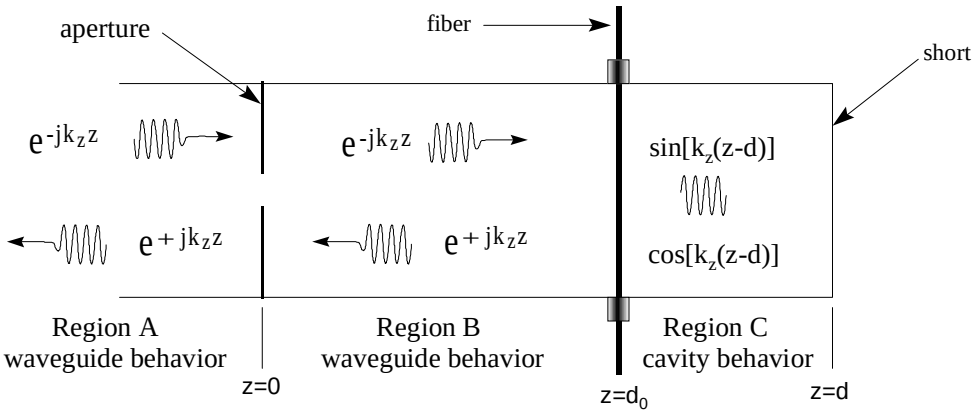

Fig. 2.3 Axial Behavior of Transverse Fields

2.3.2 Waveguide Boundary Conditions and Resultant Modes

Boundary conditions are applied in two steps to determine the unique solution to the problem. First, we obtain specific forms for the vector potential functions such that the resultant electric and magnetic fields satisfy the correct boundary conditions. The second step is to apply boundary conditions at the transverse interfaces of each region as we solve for the unknown mode amplitude coefficients.

Given two regions with material properties ϵ_1, μ_1, σ_1 and ϵ_2, μ_2, σ_2 defined on each side of a surface boundary S, the boundary conditions for the tangential fields derived from Maxwell's equations are given by

$$\begin{aligned} \hat{n} \times (\vec{E}_2 - \vec{E}_1) &= -\vec{M}_s \\ \hat{n} \times (\vec{H}_2 - \vec{H}_1) &= \vec{J}_s, \end{aligned} \tag{2.3.9}$$

where $\widehat{n}$ is the unit vector normal to the surface and directed into Region 2 [16]. The source terms are related to the physical description of the boundary and may be viewed as either impressed or induced currents. If $\vec{M}_s$ or $\vec{J}_s$ is zero, then (2.3.9) implies continuity of the tangential electric or magnetic field, respectively. This is the case at the boundary of any two materials, including perfect electric conductors (PEC). However, if one region is a PEC, (2.3.9) simplifies to

$$\begin{array}{l} \widehat{n} \times \vec{E} = 0 \\ \widehat{n} \times \vec{H} = \vec{J}_s \end{array} \quad \text{, at a PEC.} \tag{2.3.10}$$

The PEC boundary condition determines the forms of the vector potential functions for a waveguide. The eigenfunctions, dependent on transverse coordinates only, satisfy boundary conditions at the longitudinal boundaries of the waveguide. On the longitudinal PEC waveguide walls, the TE eigenfunctions satisfy the Neumann boundary condition

$$\frac{\partial \psi^h(\vec{\rho})}{\partial n} = 0. \tag{2.3.11\textit{a}}$$

Likewise, TM modes satisfy the Dirichlet boundary condition

$$\psi^e(\vec{\rho}) = 0 \tag{2.3.11\textit{b}}$$

on the waveguide walls. When these are met, the resulting electric fields tangential to the longitudinal walls satisfy the PEC condition [17]. The separation of variables solution to the scalar Helmholtz equation that satisfies (2.3.11) for Fig. 2.1 is

$$\boxed{\begin{array}{l} \psi^h_{mn} = \alpha^h_{mn} \cos\left(\frac{m\pi x}{a}\right)\cos\left(\frac{n\pi y}{b}\right) \\ \psi^e_{mn} = \alpha^e_{mn} \sin\left(\frac{m\pi x}{a}\right)\sin\left(\frac{n\pi y}{b}\right). \end{array}} \tag{2.3.12}$$

Here, α^h_{mn} and α^e_{mn} are mode normalization constants to be subsequently defined.

The z-dependent functions describing the TE and TM modes in a waveguide region satisfy the waveguide radiation condition

$$\boxed{\phi^h_w(z) = \phi^e_w(z) = \phi^{(\mp)}_{w,mn}(z) = \begin{cases} e^{-jk_{z,mn}(z-z_0)} & \text{, forward traveling wave} \\ e^{+jk_{z,mn}(z-z_0)} & \text{, backward traveling wave} \end{cases}} \tag{2.3.13}$$

where

$$k_{z,mn} = \sqrt{k^2 - \left(\frac{m\pi}{a}\right)^2 - \left(\frac{n\pi}{b}\right)^2} \tag{2.3.14}$$

and z_0 denotes the point of origin for the wave. In a cavity region, we require the transverse components of the electric field to equal zero at the shorting plane. For a short located at $z = d$, the z-dependent functions for the TE and TM modes are

$$\boxed{\begin{aligned} \phi^h_{c,mn}(z) &= \sin\left[k_{z,mn}(z-d)\right] \\ \phi^e_{c,mn}(z) &= \cos\left[k_{z,mn}(z-d)\right], \end{aligned}} \tag{2.3.15}$$

respectively.

At this point we introduce a new notation to designate waveguide mode numbers. We will commonly use the subscript ν to represent a single (m,n) combination in expressions that consist of symbolic functions. We will revert back to the (m,n) subscript designation as needed to clarify the evaluation of specific functions.

Having derived the specific forms for the potential functions, we may now define additional waveguide parameters to be used throughout the analysis. If we substitute either the TE or TM eigenfunction into (2.3.6), we find the cutoff wavenumber is

$$k^2_{c,\nu} = \left(\frac{m\pi}{a}\right)^2 + \left(\frac{n\pi}{b}\right)^2. \tag{2.3.16}$$

Expressing the time dependence of the time-harmonic fields as $e^{j\omega t}$, the propagation constant is defined as

$$k_{z,\nu} = \sqrt{k^2 - k^2_{c,\nu}} = \begin{cases} \beta & , k^2_{z,\nu} > 0 \\ -j\beta & , k^2_{z,\nu} < 0. \end{cases} \tag{2.3.17}$$

For a given wavenumber k, the mode propagation constant is only real for a finite number of modes. The mode is non-propagating, or evanescent, when $k_{z,\nu}$ is imaginary. The propagation constant of propagating modes may also be modified through a perturbational technique to include loss in the longitudinal walls. For $k_{z,\nu}$ real, we obtain

$$k_{z,\nu} = \beta - j\alpha_c, \tag{2.3.18}$$

where the loss factor is

$$\alpha_c = \frac{\mathcal{R}}{b\eta\sqrt{1-\left(\frac{f_c}{f}\right)^2}}\left[1+\frac{2b}{a}\left(\frac{f_c}{f}\right)^2\right] \tag{2.3.19}$$

and $\mathcal{R}$ is the surface resistance of the waveguide walls [16]. The surface resistance [18] within a skin depth of the surface for good conductors is given by

$$\mathcal{R} = \frac{1}{\delta_s \sigma_c} = \sqrt{\frac{\pi f \mu_c}{\sigma_c}} \simeq 0.014, \qquad \text{for copper at } f = 2.93 \text{ GHz}, \tag{2.3.20}$$

where δ_s is the skin depth in meters and σ_c is the conductivity per unit length (S/m) of the material.

Another parameter is the characteristic wave impedance that exists for each waveguide mode. The wave impedance for a TE-mode is defined as

$$Z_\nu^h = \frac{E_{x,\nu}^h}{H_{y,\nu}^h}, \tag{2.3.21}$$

where $E_{x,\nu}^h$ and $H_{y,\nu}^h$ are the TE-mode fields found from (2.3.8*b*). The wave impedance is in the z direction if we use the $\phi_\nu(z)$ for a forward traveling wave. Upon substituting this $\phi_\nu(z)$ and ψ_ν^h into (2.3.8*b*), we obtain

$$Z_\nu^h = \frac{\omega\mu}{k_{z,\nu}}. \tag{2.3.22}$$

Similarly, the wave impedance in the z direction for a TM-mode is

$$Z_\nu^e = \frac{E_{x,\nu}^e}{H_{y,\nu}^e} = \frac{k_{z,\nu}}{\omega\epsilon}. \tag{2.3.23}$$

The wave impedance for evanescent modes becomes imaginary and is inductive in nature for TE modes and capacitive for TM modes [17].

The total transverse fields can now be expressed in terms of the potential functions specific to a given region. Substituting the z-dependent functions into (2.3.8b) and evaluating the z-derivatives, we obtain the transverse fields for a waveguide region in the form

$$\vec{E}_t^{(\pm)} = \sum_\nu \big[\hat{z} \times \nabla_t \psi_\nu^h E_\nu^{h(\pm)} \mp Z_\nu^e \nabla_t \psi_\nu^e E_\nu^{e(\pm)}\big] \phi_w^{(\mp)}$$
$$\vec{H}_t^{(\pm)} = \sum_\nu \big[-\hat{z} \times \nabla_t \psi_\nu^e E_\nu^{e(\pm)} \mp \frac{1}{Z_\nu^h} \nabla_t \psi_\nu^h E_\nu^{h(\pm)}\big] \phi_w^{(\mp)}, \tag{2.3.24a}$$

where the coefficients $E_\nu^{h(\pm)}$ and $E_\nu^{e(\pm)}$ are the unknown mode amplitudes. Likewise, in a cavity region we have

$$\vec{E}_t = \sum_\nu \big[\hat{z} \times \nabla_t \psi_\nu^h E_\nu^h + j Z_\nu^e \nabla_t \psi_\nu^e E_\nu^e\big] \phi_c^h$$
$$\vec{H}_t = \sum_\nu \big[-\hat{z} \times \nabla_t \psi_\nu^e E_\nu^e - j \frac{1}{Z_\nu^h} \nabla_t \psi_\nu^h E_\nu^h\big] \phi_c^e. \tag{2.3.24b}$$

The notation is simplified by defining normal mode vectors for the TE and TM modes as

$$\vec{e}_{t,\nu}^h = \hat{z} \times \nabla_t \psi_\nu^h = \alpha_{mn}^h \hat{z} \times \nabla_t \cos\big(\frac{m\pi x}{a}\big)\cos\big(\frac{n\pi y}{b}\big)$$
$$\vec{e}_{t,\nu}^e = Z_\nu^e \nabla_t \psi_\nu^e = \alpha_{mn}^e Z_{mn}^e \nabla_t \sin\big(\frac{m\pi x}{a}\big)\sin\big(\frac{n\pi y}{b}\big) \tag{2.3.25a}$$

$$\vec{h}_{t,\nu}^h = \frac{1}{Z_\nu^h} \nabla_t \psi_\nu^h = -\frac{1}{Z_\nu^h} \hat{z} \times \vec{e}_{t,\nu}^h$$
$$\vec{h}_{t,\nu}^e = -\hat{z} \times \nabla_t \psi_\nu^e = -\frac{1}{Z_\nu^e} \hat{z} \times \vec{e}_{t,\nu}^e \tag{2.3.25b}$$

and requiring them to be orthonormal over the waveguide cross-section as

$$\int_{S_w} \vec{e}_{t,\nu}^h \cdot \vec{e}_{t,\gamma}^h ds = \delta_{\nu\gamma}$$
$$\int_{S_w} \vec{e}_{t,\nu}^e \cdot \vec{e}_{t,\gamma}^e ds = \delta_{\nu\gamma} \tag{2.3.26}$$

where S_w is the cross-section of the waveguide and $\delta_{\nu\gamma}$ is the Kronecker delta function defined as

$$\delta_{\nu\gamma} = \begin{cases} 1 & , \nu = \gamma \\ 0 & , \nu \neq \gamma. \end{cases} \tag{2.3.27}$$

Substituting for the $\vec{e}_t^h$ vectors in (2.3.26) gives

$$\int_{S_w} \vec{e}^{\,h}_{t,mn} \cdot \vec{e}^{\,h}_{t,pq} ds = \int_0^a \int_0^b (\alpha^h_{mn})^2 \Big[\Big(\frac{\pi}{b}\Big)^2 nq \cos(\frac{m\pi x}{a}) \cos(\frac{p\pi x}{a}) \sin(\frac{n\pi y}{b}) \sin(\frac{q\pi y}{b}) + \Big(\frac{\pi}{a}\Big)^2 mp \sin(\frac{m\pi x}{a}) \sin(\frac{p\pi x}{a}) \cos(\frac{n\pi y}{b}) \cos(\frac{q\pi y}{b}) \Big] dy dx$$

$$= (\alpha^h_{mn})^2 (1+\delta_{m0})(1+\delta_{n0}) \frac{ab}{4} k^2_{c,mn} \delta_{mp} \delta_{nq}. \tag{2.3.28}$$

This shows that $\vec{e}^{\,h}_{t,mn}$ is orthonormal when

$$\alpha^h_{mn} = \frac{2}{\sqrt{ab(1+\delta_{m0})(1+\delta_{n0})}\, k_{c,mn}}. \tag{2.3.29a}$$

Similarly, $\vec{e}^{\,e}_{t,mn}$ is orthonormal when

$$\alpha^e_{mn} Z^e_{mn} = \frac{2}{\sqrt{ab}\, k_{c,mn}}. \tag{2.3.29b}$$

Furthermore, $\vec{e}^{\,h}_{t,mn}$ and $\vec{e}^{\,e}_{t,mn}$ are orthogonal with respect to each other, as

$$\int_{S_w} \vec{e}^{\,h}_{t,mn} \cdot \vec{e}^{\,e}_{t,pq} ds = 0. \tag{2.3.30}$$

The normal mode vectors may now be written as

$$\begin{aligned} \vec{e}^{\,h}_{t,mn} &= \alpha^h_{mn} \Big[\widehat{x} \frac{n\pi}{b} \cos\big(\frac{m\pi x}{a}\big) \sin\big(\frac{n\pi y}{b}\big) - \widehat{y} \frac{m\pi}{a} \sin\big(\frac{m\pi x}{a}\big) \cos\big(\frac{n\pi y}{b}\big) \Big] \\ \vec{e}^{\,e}_{t,mn} &= \alpha^e_{mn} Z_{mn} \Big[\widehat{x} \frac{m\pi}{a} \cos\big(\frac{m\pi x}{a}\big) \sin\big(\frac{n\pi y}{b}\big) + \widehat{y} \frac{n\pi}{b} \sin\big(\frac{m\pi x}{a}\big) \cos\big(\frac{n\pi y}{b}\big) \Big]. \end{aligned} \tag{2.3.31}$$

The $\vec{h}$ normal mode vectors may be derived from the $\vec{e}$ normal mode vectors given above using (2.3.25*b*). A summary of the modal field solution forms is given in Table 2.1.

Table 2.1 Transverse Field Solution Forms

Modal Field Solution Forms	Type of Region
$\vec{E}^{(\pm)}_t = \sum_\nu \big[\vec{e}^{\,h}_{t,\nu} E^{h(\pm)}_\nu \mp \vec{e}^{\,e}_{t,\nu} E^{e(\pm)}_\nu \big] e^{\mp j k_{z,\nu}(z-z_0)}$ $\vec{H}^{(\pm)}_t = \sum_\nu \big[\mp \vec{h}^{\,h}_{t,\nu} E^{h(\pm)}_\nu + \vec{h}^{\,e}_{t,\nu} E^{e(\pm)}_\nu \big] e^{\mp j k_{z,\nu}(z-z_0)}$	waveguide region
$\vec{E}_t = \sum_\nu \big[\vec{e}^{\,h}_{t,\nu} E^h_\nu + j \vec{e}^{\,e}_{t,\nu} E^e_\nu \big] \sin\big[k_{z,\nu}(z-d)\big]$ $\vec{H}_t = \sum_\nu \big[-j \vec{h}^{\,h}_{t,\nu} E^h_\nu + \vec{h}^{\,e}_{t,\nu} E^e_\nu \big] \cos\big[k_{z,\nu}(z-d)\big]$	cavity region

Theoretically, the complete solution specifies every unknown amplitude coefficient in terms of the incident field. This is not possible since an infinite number of modes exist in the waveguide. Finite computational power and time result in a final solution that must inevitably be an approximation in some sense. The number of modes used will be truncated at a sufficiently high order such that the solution converges in a reasonable manner.

Before applying the modal field equations to solve the complete problem, we will first develop the fundamental methods and concepts. We will then apply these to solve for the fields in the individual aperture and fiber problems. Finally, we will combine the aperture and fiber solutions to obtain the complete solution.

2.3.3 Mode-matching Concepts

The fields developed thus far are a superposition of an infinite set of independent modes, with each mode having an unknown amplitude coefficient. Practically, we can only solve for a finite number of modes. Therefore, when we apply mode-matching to compute the coefficients, we must truncate the number of modes to given order. Given two regions in space capable of supporting modal field structures, we wish to determine each unknown amplitude in terms of one or more given mode coefficients such that the fields satisfy the boundary conditions at the interface between the two regions. To completely satisfy a boundary condition on a particular field component, we must enforce the same boundary condition on each mode describing the field. With mode-matching, we generally apply boundary condition equations at the surface interface to relate the mode coefficients of one region to another as a complete set. We will illustrate the concepts of mode-matching in the following example involving reflection and scattering of TE modes.

Consider two regions each supporting a modal type field solution. As shown in Fig. 2.4, Regions A and B are cylindrical waveguide sections with a constant cross-section S_w in the transverse coordinates. The interface surface S, separating the two regions at $z = 0$, consists of two parts: S_1 and S_2. The surface S_1 is a sub-portion of S and is defined as a PEC. Region A contains the incident mode and the modes reflected

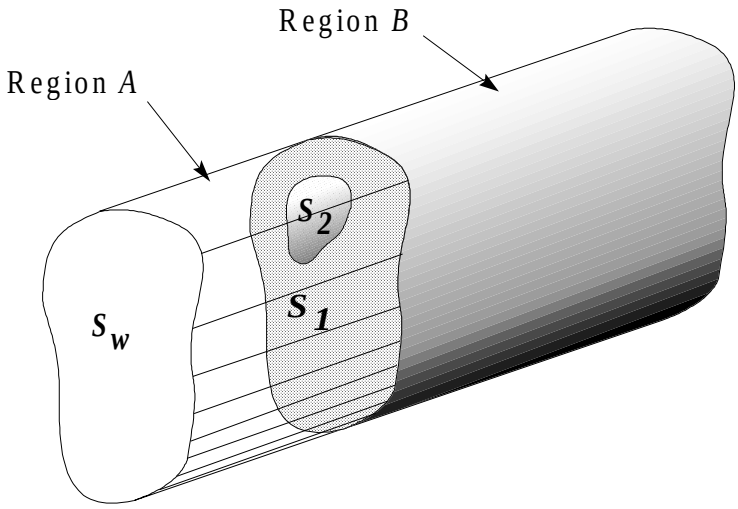

Fig. 2.4 Geometry for Aperture Mode-Matching

from the surface discontinuity. The modes in Region B are scattered from the surface. Applying only the TE-mode transverse field equations given in Tab. 2.1, the transverse fields in Regions A and B are described as

$$\begin{aligned} \vec{E}_t^A &= \sum_\nu \left(\delta_{\nu\nu_0} e^{-jk_{z,\nu_0}z} + A_\nu^h e^{+jk_{z,\nu}z}\right)\vec{e}_\nu^h \\ \vec{H}_t^A &= -\sum_\nu \left(\delta_{\nu\nu_0} e^{-jk_{z,\nu_0}z} - A_\nu^h e^{+jk_{z,\nu}z}\right)\vec{h}_{t,\nu}^h \end{aligned} \quad \text{, in Region } A \qquad (2.3.32a)$$

$$\begin{aligned} \vec{E}_t^B &= \sum_\nu B_\nu^h \vec{e}_\nu^h e^{-jk_{z,\nu}z} \\ \vec{H}_t^B &= -\sum_\nu B_\nu^h \vec{h}_{t,\nu}^h e^{-jk_{z,\nu}z} \end{aligned} \quad \text{, in Region } B, \qquad (2.3.32b)$$

where $\delta_{\nu\nu_0}$ represents the incident mode $\nu = \nu_0$ having unity amplitude, $\vec{e}_\nu$ are orthogonal mode vectors. The surface $S_2 = S - S_1$ is the remaining part and is defined as free-space.

The fields given in (2.3.32) must satisfy the boundary conditions

$$\boxed{\begin{aligned} &\text{Condition 1:} \quad \hat{z} \times \left(\vec{E}^B - \vec{E}^A\right) = 0 \quad , \text{on } S \qquad (2.3.33a) \\ &\text{Condition 2:} \quad \hat{z} \times \vec{E}^B = -\hat{z} \times \vec{E}^A = 0 \quad , \text{on } S_1 \qquad (2.3.33b) \\ &\text{Condition 3:} \quad \hat{z} \times \left(\vec{H}^B - \vec{H}^A\right) = 0 \quad , \text{on } S_2 \qquad (2.3.33c) \end{aligned}}$$

We may also use the additional boundary conditions

$$\boxed{\begin{aligned} \hat{z} \times \left(\vec{H}^B - \vec{H}^A\right) &= \vec{J}_s \quad , \text{on } S_1 \qquad (2.3.34a) \\ \hat{z} \times \vec{E}^A &= \vec{M}_s \quad , \text{on } S_2 \qquad (2.3.34b) \end{aligned}}$$

to express the fields in terms of surface currents. The magnetic surface current $\vec{M}_s$ is a fictitious source used for modeling the fields on S_2. The three basic approaches used to relate the coefficients in each region are the magnetic current method, electric current method, and direct mode-matching method. In all three cases, we apply Condition 1 as

$$\sum_\nu (\delta_{\nu\nu_0} + A_\nu^h)\vec{e}_\nu^h(\vec{\rho}) = \sum_\nu B_\nu^h \vec{e}_\nu^h(\vec{\rho}). \qquad (2.3.35)$$

This results in the relationship

$$A_\nu^h = B_\nu^h - \delta_{\nu\nu_0} \qquad (2.3.36)$$

between the mode coefficients of each region allowing us to eliminate one set of coefficients.

In the magnetic current method, we use (2.3.34*b*) along with Condition 2 to obtain

$$\hat{z} \times \sum_\nu \left[(A_\nu^h + \delta_{\nu\nu_0})\vec{e}_{t,\nu}^h \right] = \begin{cases} \vec{M}_s, & \text{on } S_2 \\ 0, & \text{on } S_1. \end{cases} \qquad (2.3.37)$$

Since the normal mode vector $\vec{e}_{t,\nu}^h$ is orthonormal, we can apply a Fourier analysis over the waveguide cross-section to determine the Region A mode coefficients in terms of the unknown magnetic current. We complete this approach by enforcing Condition 3, the continuity of the tangential magnetic field on S_2, to obtain an equation in terms of the unknown mode coefficients of Region A and Region B. Using Conditions 1 and 3, we may eliminate the Region A coefficients and express the Region B coefficients in terms of

the unknown magnetic current to obtain an equation in terms of only the magnetic surface current. In general, the resulting equation has the form

$$L\Phi = f, \tag{2.3.38}$$

where Φ represents the unknown magnetic current on S_2, f results from the incident mode, and L is a linear operator representing the mathematical operations that result from computing the relationships between the mode coefficients and the magnetic current. This equation may be easily solved using the method of moments described in the next section. Once the magnetic current is found, we may solve directly for the modal coefficients.

The electric current method is essentially the dual of the magnetic current method. In this case, we use Condition 3 along with (2.3.34*a*) to express the magnetic field in terms of an unknown electric surface current, which exists only on S_1 and is zero on S_2. Again we may eliminate the Region A coefficients using Condition 1 and obtain the Region B mode coefficients directly in terms of the electric current. We then enforce the zero tangential electric field boundary condition on S_1 using Condition 2. The resulting equation is similar to (2.3.38) except Φ would represent the unknown electric current on S_1. Again, once the electric current is known, we solve directly for the modal coefficients.

In the direct mode-matching method, we apply Condition 2 to match the modes to zero on S_1 and Condition 3 to match the modes of the two regions on S_2. If the number of waveguide modes has been truncated to order $\mathcal{N}$, then we have two equations with $\mathcal{N}$ unknowns, where the unknowns are the actual mode coefficients to be determined. We may compute the mode coefficients by choosing two sets of weighting functions over each surface, S_1 and S_2 respectively. A difficulty with this approach is the proper mix of equations for regions S_1 and S_2. The details of how these sets are chosen will not be presented here since this method is not a part of the solution at hand.

2.3.4 Method of Moments Solution

One common method used to solve for the unknown current source term, whether electric or magnetic, is the method of moments. In this method we seek an approximate solution to the operator equation

$$L\Phi = f \tag{2.3.38}$$

with Φ having the approximate form

$$\Phi \simeq \sum_{p=1}^{P} a_p u_p, \tag{2.3.39}$$

where $\{u_p\}$ is a set of independent basis functions. We choose a set of independent weighting functions $\{w_m\}$ and take the inner product of (2.3.38) with each w_m to obtain the system of linear equations

$$\boxed{\sum_{p=1}^{P} a_p < w_m, Lu_p > \; = \; < w_m, f > , \qquad m = 1, 2, \ldots, P,} \tag{2.3.40}$$

where the inner product[1] of two functions defined over S is

$$< f, g > \; = \int_S fg ds. \tag{2.3.41}$$

The unknown a_p coefficients are computed by solving the matrix equation

$$[\,A\,][\,X\,] = [\,B\,], \tag{2.3.42}$$

where the matrix elements are $A_{mp} = < w_m, Lu_p >$ and the corresponding vector elements are $B_m = < w_m, f >$ and $X_p = a_p$. This method will be applied in detail as we develop the solution at the aperture interface [19].

2.3.5 Aperture Interface

The coupling aperture, or iris, is a metal plate located in the transverse plane with an opening allowing fields to penetrate to the other side. The iris creates a non-uniform structure within the transverse plane causing higher order modes to couple into the waveguide. Depending on the dimensions of the waveguide and frequency of the modes, these will either be propagating or evanescent waves. The evanescent waves decay exponentially with distance away from the aperture and store energy in the vicinity of the aperture. The energy storage can be capacitive or inductive depending on the orientation and shape of the aperture discontinuity. Although the problem modeled here uses a TE_{10} dominant mode waveguide, this analysis is not limited to any specific parameter values.

[1]We have used the real inner product form here, since the basic mode functions are real in x and y.

This solution also allows for an arbitrarily shaped aperture, however, as we implement the solution in Chapter 3 the shape of the aperture is restricted to a rectangle of arbitrary dimensions. This simplifies the analysis while still retaining a wide range of possible configurations.

Figure 2.5 shows the general iris problem under consideration. The aperture interface located at $z = 0$ separates the waveguide into the two regions A and B. Region A is the source region extending from the iris to $z = -\infty$. This region contains an incident field propagating toward the interface and the fields reflected from the aperture propagating in the backward direction toward the source. The fields in Region B consist of scattered fields, all of which propagate in the forward direction since there are no discontinuities to cause reflections. We will use the subscript ν_0 to designate the mode number of the incident field. For a TE_{10}-mode incident field, ν_0 represents the $(m = 1, n = 0)$ mode.

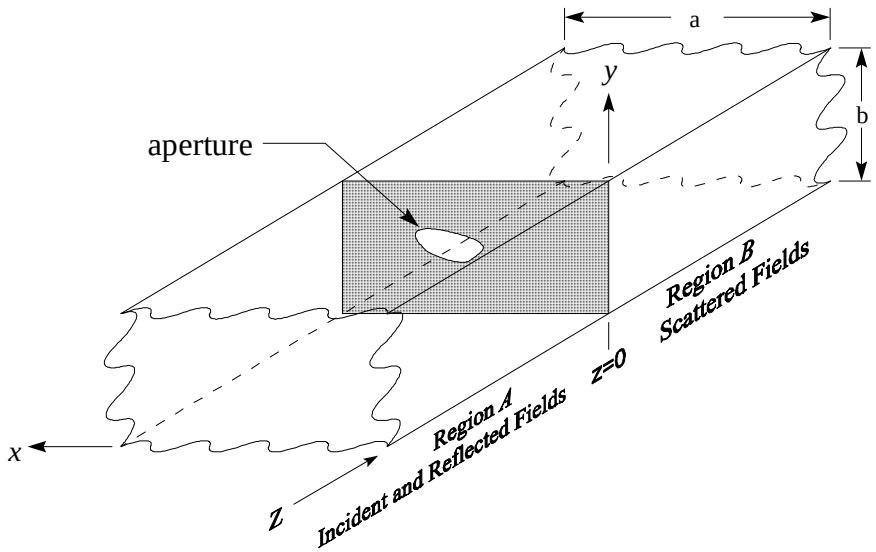

Fig. 2.5 Aperture Interface

Applying (2.3.24) to this problem we use

$$\vec{E}_{inc} = \vec{e}^{\,h}_{t,\nu_0} e^{-jk_{z,\nu_0} z}$$

to give

$$\begin{aligned} \vec{E}_t^{\,A} &= \sum_\nu \Big[\big(A^h_\nu e^{+jk_{z\nu}z} + \delta_{\nu\nu_0} e^{-jk_{z,\nu_0}z} \big) \vec{e}^{\,h}_{t,\nu} + A^e_\nu \vec{e}^{\,e}_{t,\nu} e^{+jk_{z,\nu}z} \Big] \\ \vec{H}_t^{\,A} &= \sum_\nu \Big[\big(A^h_\nu e^{+jk_{z,\nu}z} - \delta_{\nu\nu_0} e^{-jk_{z,\nu_0}z} \big) \vec{h}^{\,h}_{t,\nu} + A^e_\nu \vec{h}^{\,e}_{t,\nu} e^{+jk_{z,\nu}z} \Big] \end{aligned} \qquad (2.3.43a)$$

$$\begin{aligned} \vec{E}_t^{\,B} &= \sum_\nu \Big[\Big(B^h_\nu \vec{e}^{\,h}_{t,\nu} - B^e_\nu \vec{e}^{\,e}_{t,\nu} \Big) e^{-jk_{z,\nu}z} \Big] \\ \vec{H}_t^{\,B} &= -\sum_\nu \Big[\Big(B^h_\nu \vec{h}^{\,h}_{t,\nu} - B^e_\nu \vec{h}^{\,e}_{t,\nu} \Big) e^{-jk_{z,\nu}z} \Big] \end{aligned} \qquad (2.3.43b)$$

as the transverse field equations for each region. The solution is complete when the unknown mode coefficients are found in terms of the incident field. We will consider the magnetic current mode-matching method to compute an approximate solution to a truncated set of mode coefficients. Similarly to the method derived previously, we equate the magnetic surface current in the aperture to the modal field solution by enforcing the continuity of the tangential magnetic field in the aperture.

We can match the fields over the entire cross-section of the waveguide through the continuity of the tangential electric-field boundary condition, which is valid at any surface. At the aperture interface we apply

$$\vec{E}_t^{\,A} = \vec{E}_t^{\,B}, \quad z = 0 \qquad (2.3.44)$$

to relate the fields in the adjacent regions. Substituting the modal solutions in (2.3.44) gives

$$\sum_\nu \Big[(A^h_\nu + \delta_{\nu\nu_0}) \vec{e}^{\,h}_{t,\nu} + A^e_\nu \vec{e}^{\,e}_{t,\nu} \Big] = \sum_\nu \Big[B^h_\nu \vec{e}^{\,h}_{t,\nu} - B^e_\nu \vec{e}^{\,e}_{t,\nu} \Big]. \qquad (2.3.45)$$

Since the normal mode vectors are orthogonal, the TE and TM mode coefficients are separable and can be equated term by term giving

$$\boxed{\begin{aligned} A^h_\nu &= B^h_\nu - \delta_{\nu\nu_0} \\ A^e_\nu &= -B^e_\nu. \end{aligned}} \qquad (2.3.46)$$

The magnetic surface current is defined as

$$\hat{z} \times \vec{E} = \begin{cases} \vec{M}_s, & \text{in aperture} \\ 0, & \text{on iris} \end{cases}. \tag{2.3.47}$$

If this equality is enforced, the boundary condition for the tangential electric field will be satisfied on the iris. At the interface,

$$\hat{z} \times \sum_{\nu} \Big[\big(A^h_\nu + \delta_{\nu\nu_0}\big)\vec{e}^{\,h}_{t,mn} + A^e_{mn}\vec{e}^{\,e}_{t,mn} \Big] = \begin{cases} \vec{M}_s, & \text{in aperture} \\ 0, & \text{on iris.} \end{cases} \tag{2.3.48}$$

The orthonormality of the normal mode vectors allows us to determine the Region A mode coefficients by using a Fourier analysis giving

$$\begin{aligned} A^h_\nu &= \int_{S_a} \vec{M}_s \cdot \big(\hat{z} \times \vec{e}^{\,h}_{t,\nu}\big) ds - \delta_{\nu\nu_0} \\ A^e_\nu &= \int_{S_a} \vec{M}_s \cdot \big(\hat{z} \times \vec{e}^{\,e}_{t,\nu}\big) ds, \end{aligned} \tag{2.3.49}$$

where S_a is the aperture surface. Since the magnetic current is zero on the iris, the limits of integration are confined only to the aperture region. This indirectly satisfies the boundary condition for the tangential electric field on the iris.

The remaining boundary condition is to enforce the continuity of the tangential magnetic field in the aperture, or

$$\hat{z} \times \big(\vec{H}^B - \vec{H}^A\big) = 0, \quad \text{in aperture.} \tag{2.3.50}$$

Substituting the modal solution of the magnetic field into (2.3.50) and using (2.3.46) to eliminate the Region A coefficients gives

$$\hat{z} \times 2\sum_{\nu} \Big[\Big(B^h_\nu - \delta_{\nu 0}\Big)\vec{h}^{\,h}_{t,\nu} - B^e_\nu \vec{h}^{\,e}_{t,\nu} \Big] = 0, \quad \text{in aperture.} \tag{2.3.51}$$

Expressing the $\vec{h}$ mode normal vectors in terms of $\vec{e}$ mode normal vectors simplifies this to

$$\sum_{\nu} \Big[k_{z,\nu} B^h_\nu \vec{e}^{\,h}_{t,\nu} - \frac{k^2}{k_{z,\nu}} B^e_\nu \vec{e}^{\,e}_{t,\nu} \Big] = k_{z,\nu_0} \vec{e}^{\,h}_{t,\nu_0}, \qquad \text{in aperture.} \tag{2.3.52}$$

Furthermore, the Region B coefficients can be expressed in terms of the magnetic current integrated over the aperture. Using (2.3.46) and (2.3.49) we write this as

$$B_\nu^h = \int_{S_a} \vec{M}_s \cdot (\hat{z} \times \vec{e}_{t,\nu}^h) ds$$
$$B_\nu^e = -\int_{S_a} \vec{M}_s \cdot (\hat{z} \times \vec{e}_{t,\nu}^e) ds, \tag{2.3.53}$$

which may be substituted into (2.3.52) to obtain

$$\boxed{k_{z,\nu_0} \vec{e}_{t,\nu_0}^h = \int_{S_a} \vec{M}_s(\vec{\rho}') \cdot \hat{z} \times \sum_\nu \left[k_{z,\nu} \vec{e}_{t,\nu}^h(\vec{\rho}') \vec{e}_{t,\nu}^h(\vec{\rho}) + \frac{k^2}{k_{z,\nu}} \vec{e}_{t,\nu}^e(\vec{\rho}') \vec{e}_{t,\nu}^e(\vec{\rho}) \right] ds'.} \tag{2.3.54}$$

This expression represents a series type dyadic Green's function formulation for the aperture magnetic current in the waveguide having the form

$$\boxed{\overline{f} = \int_{S_a} \overline{M}_s(\vec{\rho}') \cdot \overline{\overline{G}}(\vec{\rho}', \vec{\rho}) ds'.} \tag{2.3.55}$$

The integral equation above is a vector form of the Fredholm equation of the first kind [19]. Once the magnetic current is obtained, the problem is complete since the mode coefficients are computed directly from the magnetic current.

We can apply the method of moments solution developed in Section 2.3.4 to the dyadic Green's function for the aperture in a similar manner. Here, L is the linear operator given by

$$L(\,) = \int_{S_a} (\,) \cdot \overline{\overline{G}}(\vec{\rho}', \vec{\rho}) ds'. \tag{2.3.56}$$

We can approximate the magnetic current with a truncated set of independent basis functions as

$$\overline{M}_s(\vec{\rho}') \simeq \sum_p^P \left[a_{p_x} u_{p_x}(\vec{\rho}') \hat{x} + a_{p_y} u_{p_y}(\vec{\rho}') \hat{y} \right]. \tag{2.3.57}$$

Since L is a linear operator,

$$L(\overline{M}_s) = \sum_p^P \left[a_{p_x} L(u_{p_x}) \hat{x} + a_{p_y} L(u_{p_y}) \hat{y} \right]. \tag{2.3.58}$$

Substituting for the magnetic current in (2.3.55) gives

$$\overline{f}(\vec{\rho}) = \sum_p^P \left[a_{p_x} \vec{F}_{p_x}(\vec{\rho}) + a_{p_y} \vec{F}_{p_y}(\vec{\rho}) \right], \tag{2.3.59}$$

where

$$\begin{aligned}\vec{F}_{p_x}(\vec{\rho}) &= L(u_{p_x}\widehat{x}) = \int_{S_a} u_{p_x}(\vec{\rho}')\left[G_{xx}(\vec{\rho}',\vec{\rho})\widehat{x} + G_{xy}(\vec{\rho}',\vec{\rho})\widehat{y}\right]ds' \\ \vec{F}_{p_y}(\vec{\rho}) &= L(u_{p_y}\widehat{y}) = \int_{S_a} u_{p_y}(\vec{\rho}')\left[G_{yx}(\vec{\rho}',\vec{\rho})\widehat{x} + G_{yy}(\vec{\rho}',\vec{\rho})\widehat{y}\right]ds',\end{aligned} \tag{2.3.60a}$$

and

$$\begin{aligned}\vec{F}_{p_x} &= F_{p_{xx}}\widehat{x} + F_{p_{xy}}\widehat{y} \\ \vec{F}_{p_y} &= F_{p_{yx}}\widehat{x} + F_{p_{yy}}\widehat{y}.\end{aligned} \tag{2.3.60b}$$

If we choose an independent weighting function set given by

$$\overline{w}_s(\vec{\rho}) = w_{s_x}(\vec{\rho})\widehat{x} + w_{s_y}(\vec{\rho})\widehat{y}, \qquad s = 1, 2, \ldots, P \tag{2.3.61}$$

and take the inner product of each component of $\overline{w}_s$ with (2.3.59), we obtain

$$\begin{aligned} &< w_{s_x}, \sum_p^P \left(a_{p_x}F_{p_{xx}} + a_{p_y}F_{p_{yx}}\right) > \; = \; < w_{s_x}, f_x > \\ &< w_{s_y}, \sum_p^P \left(a_{p_x}F_{p_{xy}} + a_{p_y}F_{p_{yy}}\right) > \; = \; < w_{s_y}, f_y > , \end{aligned} \tag{2.3.62}$$

which is a set of $2P$ equations with $2P$ unknowns. Casting (2.3.62) into a partitioned matrix form gives

$$\begin{bmatrix} < w_{s_x}, F_{1_{xx}} > \cdots < w_{s_x}, F_{P_{xx}} > & < w_{s_x}, F_{1_{yx}} > \cdots < w_{s_x}, F_{P_{yx}} > \\ \vdots \qquad\qquad\qquad \vdots & \vdots \qquad\qquad\qquad \vdots \\ < w_{P_x}, F_{1_{xx}} > \cdots < w_{P_x}, F_{P_{xx}} > & < w_{P_x}, F_{1_{yx}} > \cdots < w_{P_x}, F_{P_{yx}} > \\ \\ < w_{s_y}, F_{1_{xy}} > \cdots < w_{s_y}, F_{P_{xy}} > & < w_{s_y}, F_{1_{yy}} > \cdots < w_{s_y}, F_{P_{yy}} > \\ \vdots \qquad\qquad\qquad \vdots & \vdots \qquad\qquad\qquad \vdots \\ < w_{P_y}, F_{1_{xy}} > \cdots < w_{P_y}, F_{P_{xy}} > & < w_{P_y}, F_{1_{yy}} > \cdots < w_{P_y}, F_{P_{yy}} > \end{bmatrix} \begin{bmatrix} a_{1_x} \\ \vdots \\ a_{P_x} \\ \\ a_{1_y} \\ \vdots \\ a_{P_y} \end{bmatrix}$$

$$= \begin{bmatrix} < w_{s_x}, f_x > \\ \vdots \\ < w_{P_x}, f_x > \\ \\ < w_{s_y}, f_y > \\ \vdots \\ < w_{P_y}, f_y > \end{bmatrix}, \tag{2.3.63}$$

which is a matrix equation of the form $[A][X] = [B]$ containing $2P$ equations and $2P$ unknowns. The unknown a_p coefficients can now be computed as $[X] = [A]^{-1}[B]$. The

unknown mode amplitudes A_ν^h and A_ν^e are found directly from the approximate magnetic current. It should be noted that the independence of the basis and weighting functions in this section is with respect to the aperture. The implementation of specific basis and weighting functions is presented in Chapter 3.

2.3.6 Fiber Interface

In this section we will develop a method to compute the reflected fields in terms of the fields incident on a thin ceramic fiber in an open-ended waveguide. The fiber is modeled as a cylindrical dielectric rod having a sufficiently small cross-section that we can approximate the tangential electric fields as continuous at the interface. The rod is treated as a line source with a current proportional to the equivalent volume current density and the cross-sectional area. This equivalent line source is used to apply the boundary conditions on the tangential magnetic fields at the fiber interface.

Figure 2.6 shows the problem under consideration. The geometry is again divided into two solution regions. Region B contains the forward propagating incident modes and the backward propagating reflected modes and region C contains the forward traveling scattered modes. The effects of the shorting plane in the cavity problem are treated in a later section when the full solution is discussed.

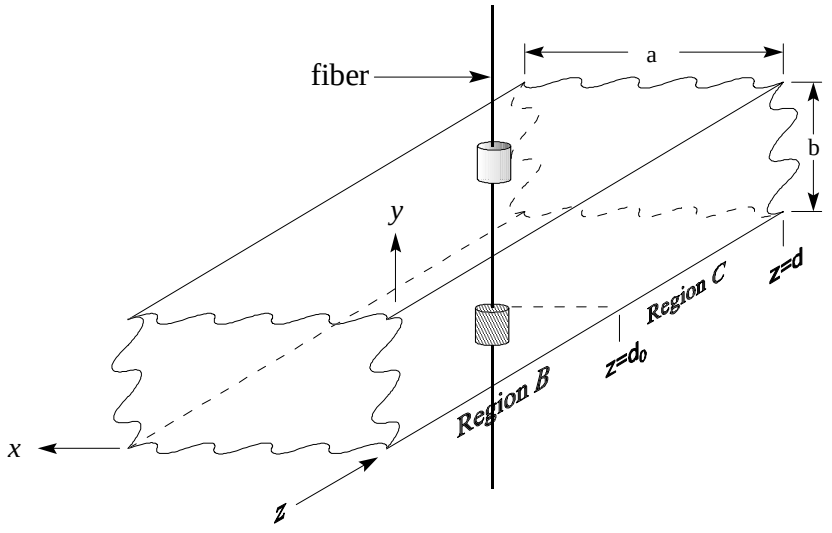

Fig. 2.6 Fiber Interface

The modal form of solution for the fields in the two regions are given as

$$\vec{E}_t^{\,B} = \sum_\nu \Big[\big(B_\nu^{h(+)} e^{-jk_{z,\nu}z} + B_\nu^{h(-)} e^{+jk_{z,\nu}(z-d_0)}\big)\vec{e}_{t,\nu}^{\,h} - \big(B_\nu^{e(+)} e^{-jk_{z,\nu}z} - B_\nu^{e(-)} e^{+jk_{z,\nu}(z-d_0)}\big)\vec{e}_{t,\nu}^{\,e} \Big] \tag{2.3.64a}$$

$$\vec{H}_t^{\,B} = -\sum_\nu \Big[\big(B_\nu^{h(+)} e^{-jk_{z,\nu}z} - B_\nu^{h(-)} e^{+jk_{z,\nu}(z-d_0)}\big)\vec{h}_{t,\nu}^{\,h} - \big(B_\nu^{e(+)} e^{-jk_{z,\nu}z} + B_\nu^{e(-)} e^{+jk_{z,\nu}(z-d_0)}\big)\vec{h}_{t,\nu}^{\,e} \Big] \tag{2.3.64b}$$

$$\vec{E}_t^{\,C} = \sum_\nu \Big[\Big(C_\nu^h \vec{e}_{t,\nu}^{\,h} - C_\nu^e \vec{e}_{t,\nu}^{\,e}\Big) e^{-jk_{z,\nu}(z-d_0)} \Big] \tag{2.3.64c}$$

$$\vec{H}_t^{\,C} = -\sum_\nu \Big[\big(C_\nu^h \vec{h}_{t,\nu}^{\,h} - C_\nu^e \vec{h}_{t,\nu}^{\,e}\big) e^{-jk_{z,\nu}(z-d_0)} \Big], \tag{2.3.64d}$$

where the $(+)$ and $(-)$ superscripts denote coefficients of the forward and backward traveling modes, respectively. The axis of the fiber is located at $x = a_0$, $z = d_0$, and extends vertically from $y = 0$ to $y = b$. Properties that define the fiber for this analysis are its diameter and relative permittivity, ϵ_r. The relative permittivity may be complex and possibly a function of y. We must now develop the approximations required to apply the appropriate boundary conditions at the fiber interface.

To determine the scattered fields, we replace the volume occupied by the fiber with the volume equivalent electric current density

$$\boxed{\vec{J}_{eq} = j\omega\big(\epsilon_r - 1\big)\epsilon_0 \vec{E} = Y\vec{E},} \tag{2.3.65}$$

which is non-zero only within the fiber [15]. The admittance parameter Y has been defined for convenience of notation as

$$Y = j\omega\big(\epsilon_r - 1\big)\epsilon_0. \tag{2.3.66}$$

Since the fiber is orientated in the y-direction, we will assume that the current only exists in this direction and therefore only consider the y-component of the electric field. In this analysis, we approximate the y-component of the electric field tangential to the fiber as constant and continuous throughout the interior of the fiber. This is valid as long as the cross-section of the fiber is small with respect to wavelength. Obstacles that exhibit this type of behavior are called Rayleigh scatterers. As the thickness of the fiber increases, the phase change in the field becomes more significant and the tangential fields would vary

throughout the fiber. When the fiber is a lossy material, the amplitude of the field would also decay according to the complex propagation constant. Therefore, if the cross-section of the fiber is much smaller than its effective skin depth, the amplitude decay is insignificant. In addition, we are assuming that any higher order modes supported by the fiber in its interior are negligible. This approximation allows us to evaluate the y-component of the electric field as constant in the x and z directions within the fiber. Furthermore, we may express the total current flowing in the y direction as

$$I_y \simeq \int_{S_f} \hat{y} \cdot \vec{J}_{eq} ds = A_f Y E_{0y}, \tag{2.3.67}$$

where S_f is the cross-section of the fiber, E_{0y} is the y-component of the electric field evaluated at the fiber axis, and A_f is the cross-sectional area of the fiber. If this current is restricted to exist only at $x = a_0$, then we may define a surface current

$$\boxed{\vec{J}_s = \hat{y} A_f Y E_{0y} \delta\big(x - a_0\big).} \tag{2.3.68}$$

We may now apply the boundary condition

$$\hat{z} \times \big(\vec{H}^C - \vec{H}^B\big) = \vec{J}_s \tag{2.3.69}$$

at the fiber interface. This equation provides the basis for developing a mode-matching solution similar to the electric current method introduced in Section 2.3.3.

As in the aperture solution, we can eliminate one set of unknowns by applying the boundary condition on the continuity of the tangential electric field at $z = d_0$ to relate the Region C coefficients to the Region B coefficients. Once again the TE and TM mode coefficients are separable and may be equated term by term giving

$$\begin{aligned} C_\nu^h &= \big(B_\nu^{h(+)} e^{-jk_{z,\nu} d_0} + B_\nu^{h(-)}\big) \\ C_\nu^e &= \big(B_\nu^{e(+)} e^{-jk_{z,\nu} d_0} - B_\nu^{e(-)}\big). \end{aligned} \tag{2.3.70}$$

Substituting in the modal solutions for the tangential magnetic fields at the fiber interface and using (2.3.70), (2.3.69) becomes

$$\vec{J}_s = \hat{z} \times \big(\vec{H}^C - \vec{H}^B\big) = -2 \sum_\nu \Big[\frac{1}{Z_\nu^h} B_\nu^{h(-)} \vec{e}_{t,\nu}^{\,h} + \frac{1}{Z_\nu^e} B_\nu^{e(-)} \vec{e}_{t,\nu}^{\,e} \Big] \tag{2.3.71}$$

If we define the coefficients

$$
\begin{aligned}
H_\nu^h &= -\frac{2}{Z_\nu^h} B_\nu^{h(-)} \\
H_\nu^e &= -\frac{2}{Z_\nu^e} B_\nu^{e(-)}
\end{aligned}
\tag{2.3.72}
$$

and substitute for $\vec{J}_s$, we can write (2.3.71) as

$$
\sum_\nu \Big[H_\nu^h \vec{e}_{t,\nu}^{\,h} + H_\nu^e \vec{e}_{t,\nu}^{\,e} \Big] = \widehat{y}\big(\widehat{y} \cdot Y \vec{E}_{0t}^{\,B}\big) A_f \delta\big(x - a_0\big). \tag{2.3.73}
$$

Applying a Fourier analysis, the mode coefficients are found to be

$$
\begin{aligned}
B_\nu^{h(-)} &= -\frac{Z_\nu^h}{2} \int_{S_w} \Big[e_{y,\nu}^h E_{0y}^B Y A_f \delta\big(x - a_0\big) \Big] ds \\
B_\nu^{e(-)} &= -\frac{Z_\nu^e}{2} \int_{S_w} \Big[e_{y,\nu}^e E_{0y}^B Y A_f \delta\big(x - a_0\big) \Big] ds,
\end{aligned}
\tag{2.3.74}
$$

where the subscript y denotes the y-component of the vector. Expanding the electric field term E_{0y}^B in the above integrals gives

$$
\begin{aligned}
B_\nu^{h(-)} = -\frac{Z_\nu^h}{2} \int_{S_w} \Big[Y A_f \delta\big(x - a_0\big) e_{y,\nu}^h \sum_\gamma \Big\{ & e_{0y,\gamma}^h \big(B_\gamma^{h(+)} e^{-jk_{z,\gamma} d_0} + B_\gamma^{h(-)} \big) \\
& - e_{0y,\gamma}^e \big(B_\gamma^{e(+)} e^{-jk_{z,\gamma} d_0} - B_\gamma^{e(-)} \big) \Big\} \Big] ds
\end{aligned}
\tag{2.3.75a}
$$

$$
\begin{aligned}
B_\nu^{e(-)} = -\frac{Z_\nu^e}{2} \int_{S_w} \Big[Y A_f \delta\big(x - a_0\big) e_{y,\nu}^e \sum_\gamma \Big\{ & e_{0y,\gamma}^h \big(B_\gamma^{h(+)} e^{-jk_{z,\gamma} d_0} + B_\gamma^{h(-)} \big) \\
& - e_{0y,\gamma}^e \big(B_\gamma^{e(+)} e^{-jk_{z,\gamma} d_0} - B_\gamma^{e(-)} \big) \Big\} \Big] ds
\end{aligned}
\tag{2.3.75b}
$$

where γ assumes the same range of values as ν. If the number of modes is truncated at $\nu = \mathcal{N}$, then (2.3.75) is a set of $2\mathcal{N}$ equations with $4\mathcal{N}$ unknowns. This allows us to find the mode coefficients for the backward traveling waves in terms of the coefficients for the forward traveling waves, which is the desired result.

A convenient method of solving for the desired relationships is to cast (2.3.75) into a matrix equation partitioned into sub-matrices as

$$
\begin{bmatrix} [0] \\ [0] \end{bmatrix} = \begin{bmatrix} [M_1^{(+)}] & [M_2^{(+)}] \\ [M_3^{(+)}] & [M_4^{(+)}] \end{bmatrix} \begin{bmatrix} [B^{h(+)}] \\ [B^{e(+)}] \end{bmatrix} + \begin{bmatrix} [M_1^{(-)}] & [M_2^{(-)}] \\ [M_3^{(-)}] & [M_4^{(-)}] \end{bmatrix} \begin{bmatrix} [B^{h(-)}] \\ [B^{e(-)}] \end{bmatrix}. \tag{2.3.76}
$$

Using ν as the row index and γ as the column index, the elements of the sub-matrices are

$$
\begin{aligned}
M^{(+)}_{1,\nu\gamma} &= Z^h_\nu \mathcal{I}^{hh}_{\nu\gamma} e^{-jk_{z,\gamma}d_0} & M^{(-)}_{1,\nu\gamma} &= Z^h_\nu \mathcal{I}^{hh}_{\nu\gamma} + \delta_{\nu\gamma} \\
M^{(+)}_{2,\nu\gamma} &= -Z^h_\nu \mathcal{I}^{he}_{\nu\gamma} e^{-jk_{z,\gamma}d_0} & M^{(-)}_{2,\nu\gamma} &= Z^h_\nu \mathcal{I}^{he}_{\nu\gamma} \\
M^{(+)}_{3,\nu\gamma} &= Z^e_\nu \mathcal{I}^{eh}_{\nu\gamma} e^{-jk_{z,\gamma}d_0} & M^{(-)}_{3,\nu\gamma} &= Z^e_\nu \mathcal{I}^{eh}_{\nu\gamma} \\
M^{(+)}_{4,\nu\gamma} &= -Z^e_\nu \mathcal{I}^{ee}_{\nu\gamma} e^{-jk_{z,\gamma}d_0} & M^{(-)}_{4,\nu\gamma} &= Z^e_\nu \mathcal{I}^{ee}_{\nu\gamma} + \delta_{\nu\gamma}
\end{aligned}
\tag{2.3.77}
$$

$$
\mathcal{I}^{\overset{h}{e}\overset{h}{e}}_{\nu\gamma} = \frac{A_f}{2}\int_{S_w} \overset{h}{e}{}^{e}_{y,\nu} \overset{h}{e}{}^{e}_{0y,\gamma} Y(y)\delta(x-a_0)\,ds,
$$

where $\nu = 1, 2, \ldots, \mathcal{N}$ and $\gamma = 1, \ldots, \mathcal{N}$. The Kronecker delta function has been used to combine like terms on the left and right-hand sides of (2.3.75). The matrix equation (2.3.76) is of the form $[0] = [M^{(+)}][B^{(+)}] + [M^{(-)}][B^{(-)}]$ which we can solve for the desired relationship as

$$
\boxed{\begin{aligned} [B^{(-)}] &= [M][B^{(+)}] \\ [M] &= -[M^{(-)}]^{-1}[M^{(+)}] \end{aligned}}
\tag{2.3.78}
$$

once the elements of the sub-matrices are known. To compute these elements, we must evaluate the integrals in (2.3.77).

From (2.3.31), the y-components of the TE and TM normal mode vectors are proportional to each other as

$$
e^e_{y,mn} = -Z^e_{mn}\frac{\alpha^e_{mn} an}{\alpha^h_{mn} bm} e^h_{y,mn} = -\frac{an}{bm} e^h_{y,mn}. \tag{2.3.79}
$$

This leaves us with only one form of integral to evaluate in (2.3.77). The elements of the sub-matrices are then simply scaled by the constant appropriate to the given mode. Let

$$
\mathcal{I}^{hh}_{\nu\gamma} = \frac{A_f}{2}\int_{S_w} e^h_{y,\nu} e^h_{0y,\gamma} Y(y)\delta(x-a_0)\,ds \tag{2.3.80}
$$

be the base integral form to evaluate. Substituting in for the normal mode vectors gives

$$
\mathcal{I}_{mnst} = \frac{A_f}{2}\alpha^h_{mn}\alpha^h_{st}\left(\frac{m\pi}{a}\right)^2 \sin\left(\frac{s\pi a_0}{a}\right)\int_0^a\int_0^b Y\delta(x-a_0)\sin\left(\frac{m\pi x}{a}\right)\cos\left(\frac{n\pi y}{b}\right)\cos\left(\frac{t\pi y}{b}\right)dydx, \tag{2.3.81}
$$

where ν and γ have been replaced by (*m*,*n*) and (*s*,*t*), respectively. The delta distribution leads to a trivial integration in x giving us only

$$\boxed{\int_0^b Y(y)\cos\left(\frac{n\pi y}{b}\right)\cos\left(\frac{t\pi y}{b}\right)dy} \tag{2.3.82}$$

to evaluate.

The admittance term $Y(y)$ introduces the temperature-dependent nature of the field solution. Since the relative permittivity used to model the fiber is temperature-dependent, any temperature variation in y causes the fiber to become an inhomogeneous material. We will investigate how to model the inhomogeneous fiber and evaluate (2.3.82) in Chapter 3. Once we evaluate this integral, we can fill the matrices of (2.3.78) and solve for the amplitudes of the reflected modes in terms of the modes incident on the fiber. We will use this relationship to modify the general aperture solution developed in Section 2.3.5 to account for the backward traveling modes scattered by the fiber.

2.4 Thermal Solution Considerations

The thermal model that describes the heating of the fiber as it is exposed to microwave energy is important to the development of the electric field solution. The source term of the heat conduction equation

$$\dot{q}(T) = \omega\epsilon_0\epsilon_r''(T,y)|E_y(y)|^2 \tag{2.4.1}$$

describes the coupling of the electromagnetic behavior to the thermal solution [3]. One possibility is to solve the two problems simultaneously using a numerical technique such as the finite-difference time-domain (FDTD) method. However, this proves to be computationally inefficient since the time-scale of the electromagnetic problem is much smaller than that of the thermal problem. Alternatively, we can solve for the electric field at a given temperature and update the thermal solution accordingly. Since the thermal solution varies much slower in time than the electromagnetic solution, it is possible to approximate the temperature distribution as constant over the time period required for the electric field to adjust itself. When the temperature profile changes enough to affect the electromagnetic solution based on a set criterion, the electric field is computed and again updates the thermal solution [9]. An FDTD solution to the heat transfer problem, such as that developed by Goodson [3], provides a temperature distribution at discrete points in space. The relative permittivity of the fiber varies in position as a function of the

temperature distribution along the fiber resulting in an inhomogeneous material. Taking temperature samples along the axis of the fiber provide a method of modeling the fiber as a set of discrete homogeneous segments. This approach is discussed in detail in Section 3.2.

2.4.1 Material Properties

The specific data used in this analysis to model the fiber are the dielectric properties for mullite, a type of metal-oxide ceramic. The dielectric loss for mullite is obtained from an interpolation subroutine developed by Goodson based on measured data [3]. This subroutine computes the values of the dielectric loss for a given temperature. The temperature-dependent dielectric constant data for mullite is found from a plot of measured data points [3]. Figures 2.7a and 2.7b show the measured dielectric constant and dielectric loss, respectively, versus temperature for mullite. The solid line shown in the plot of the dielectric constant is a second order polynomial curve fit. As shown in the plots, a relatively small increase in temperature may result in a relatively large increase in the relative permittivity at higher temperatures.

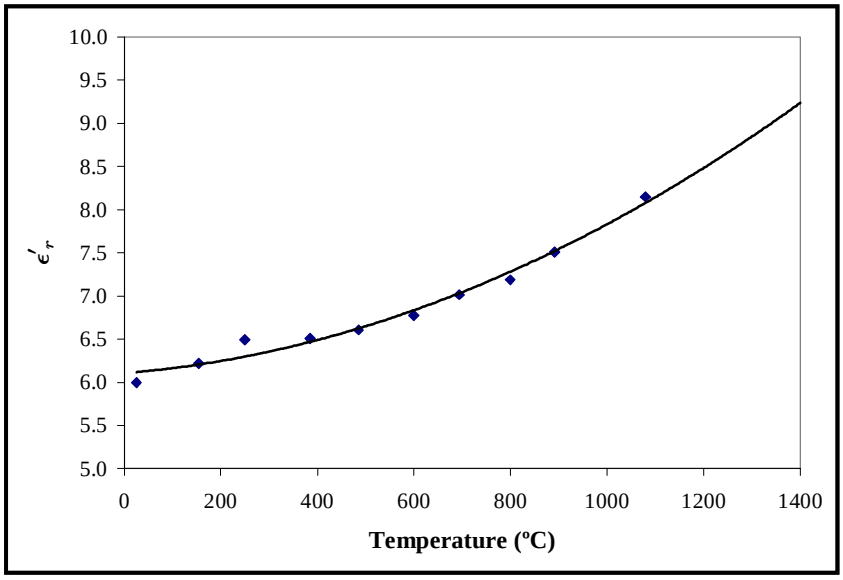

Fig. 2.7a Dielectric Constant of Mullite vs. Temperature

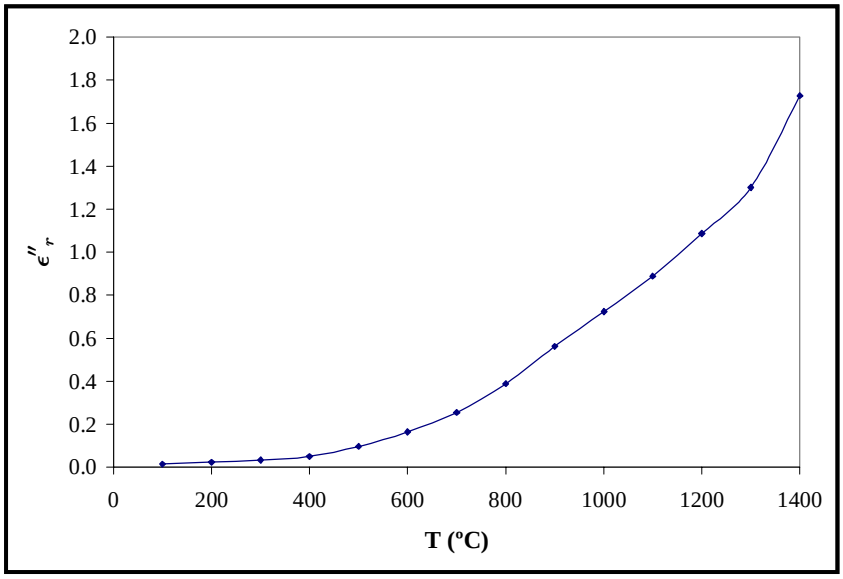

Fig. 2.7*b* Dielectric Loss of Mullite vs. Temperature

3. Application of Solution

3.0 Chapter Overview

The solution forms developed in Chapter 2 are all expressed as symbolic equations. In this chapter, we will apply these solutions to a real problem and attempt to verify our results. One method of verification is to compute the aperture and fiber impedances and compare to published results. An example of such results can be found in [20] which contains equivalent transmission line circuit parameters of obstacles in a rectangular waveguide such as inductive and capacitive irises, circular apertures, and dielectric cylinders. The solution to the complete problem is also developed by modifying the aperture and fiber solutions to account for backward traveling modes which arise from the fiber and shorting plane. The effects of incorporating an inhomogeneous fiber material is also included.

3.1 Aperture Solution

In Section 2.3.5, we developed a series type dyadic Green's function for an aperture in an open-ended waveguide. Using the method of moments, we solved for an approximation to the magnetic current which in turn was used to compute the unknown mode amplitude coefficients. This approach provides a basis for a conceptual understanding of how the problem is solved, but is difficult to implement in the full problem where the fiber causes backward traveling modes to arise. In this section, a more straightforward approach is presented by developing the solution of Section 2.3.5 entirely in a matrix form. This approach allows us to solve complicated systems of equations with simple matrix manipulation.

The matrix equations that follow all consist of partitioned matrices. For example, mode coefficients in the notation

$$\begin{bmatrix} B_\nu^h \\ B_\nu^e \end{bmatrix}$$

represents a $2\mathcal{N} \times 1$ matrix, where $\mathcal{N}$ denote the total number of waveguide modes used. The multiplication

$$[\,u_p\,][\,a_p\,]$$

represents a $[1 \times P][P \times 1]$ matrix multiplication and is equivalent to the summation $\sum_p u_p a_p$.

Substituting in the approximate magnetic current given by (2.3.56) we can write (2.3.49) as

$$\begin{aligned} A_\nu^h + \delta_{\nu\nu_0} &= \sum_{p=1}^{P} \int_{S_a} \Big(- a_{p_x} u_{p_x} e_{y,\nu}^h + a_{p_y} u_{p_y} e_{x,\nu}^h \Big) ds \\ A_\nu^e &= \sum_{p=1}^{P} \int_{S_a} \Big(- a_{p_x} u_{p_x} e_{y,\nu}^e + a_{p_y} u_{p_y} e_{x,\nu}^e \Big) ds. \end{aligned} \tag{3.1.1}$$

Using (2.3.46) to relate the Region A and Region B coefficients, we can express this as

$$\begin{aligned} B_\nu^h &= \sum_{p=1}^{P} \int_{S_a} \Big(- a_{p_x} u_{p_x} e_{y,\nu}^h + a_{p_y} u_{p_y} e_{x,\nu}^h \Big) ds \\ B_\nu^e &= \sum_{p=1}^{P} \int_{S_a} \Big(a_{p_x} u_{p_x} e_{y,\nu}^e - a_{p_y} u_{p_y} e_{x,\nu}^e \Big) ds. \end{aligned} \tag{3.1.2}$$

Since $\nu = 1, 2, \ldots, \mathcal{N}$, (3.1.2) really represents $2\mathcal{N}$ equations each having $2P$ unknowns. It is also worthwhile to point out that the subscripts for the TM modes are over the same range as the TE modes despite the fact that TM_{m0} modes do not exist. In this case, the amplitudes are simply taken to be zero. We can cast this into a partitioned matrix form as

$$\begin{bmatrix} B_\nu^h \\ B_\nu^e \end{bmatrix} = \begin{bmatrix} -\int_{S_a} u_{p_x} e_{y,\nu}^h ds & \int_{S_a} u_{p_y} e_{x,\nu}^h ds \\ \int_{S_a} u_{p_x} e_{y,\nu}^e ds & -\int_{S_a} u_{p_y} e_{x,\nu}^e ds \end{bmatrix} \begin{bmatrix} a_{p_x} \\ a_{p_y} \end{bmatrix}. \tag{3.1.3}$$

We see from (3.1.2) that once the expansion function amplitudes, $\big[a_p\big]$, are determined and the integrals are evaluated, the mode coefficients are found by a simple matrix multiplication.

In Section 2.3.5, the continuity of the tangential magnetic field in the aperture led to

$$\sum_{\nu}\left[k_{z,\nu}B^h_\nu\vec{e}^h_{t,\nu}-\frac{k^2}{k_{z,\nu}}B^e_\nu\vec{e}^e_{t,\nu}\right]=k_{z,\nu_0}\vec{e}^h_{t,\nu_0},\qquad\text{in aperture.}\tag{2.3.52}$$

Taking the inner product of the weighting functions with this equation and casting it in matrix form with the x and y components partitioned into separate rows gives us

$$\begin{bmatrix}k_{z,\nu}\int_{S_a}w_{s_x}e^h_{x,\nu}ds & -\frac{k^2}{k_{z,\nu}}\int_{S_a}w_{s_x}e^e_{x,\nu}ds\\ k_{z,\nu}\int_{S_a}w_{s_y}e^h_{y,\nu}ds & -\frac{k^2}{k_{z,\nu}}\int_{S_a}w_{s_y}e^e_{y,\nu}ds\end{bmatrix}\begin{bmatrix}B^h_\nu\\B^e_\nu\end{bmatrix}=\begin{bmatrix}k_{z,\nu_0}\int_{S_a}w_{s_x}e^h_{x,\nu_0}ds\\k_{z,\nu_0}\int_{S_a}w_{s_y}e^h_{y,\nu_0}ds\end{bmatrix},\quad\text{in aperture,}\tag{3.1.4}$$

where the subscript $s=1,2,\ldots,P$. It is worth noting that the $\left[B\right]$ coefficients can not be solved directly by inversion in (3.1.4) because the waveguide modes are not defined over the same region as the aperture modes. Hence, the matrix that pre-multiplies the $\left[B\right]$ coefficients in (3.1.4) is not square. Upon substituting (3.1.3) into (3.1.4) we obtain

$$[A][X]=[F],\tag{3.1.5}$$

where

$$[A]=\begin{bmatrix}k_{z,\nu}\int_{S_a}w_{s_x}e^h_{x,\nu}ds & -\frac{k^2}{k_{z,\nu}}\int_{S_a}w_{s_x}e^e_{x,\nu}ds\\ k_{z,\nu}\int_{S_a}w_{s_y}e^h_{y,\nu}ds & -\frac{k^2}{k_{z,\nu}}\int_{S_a}w_{s_y}e^e_{y,\nu}ds\end{bmatrix}\begin{bmatrix}-\int_{S_a}u_{p_x}e^h_{y,\nu}ds & \int_{S_a}u_{p_y}e^h_{x,\nu}ds\\ \int_{S_a}u_{p_x}e^e_{y,\nu}ds & -\int_{S_a}u_{p_y}e^e_{x,\nu}ds\end{bmatrix},$$

$$[X]=\begin{bmatrix}a_{p_x}\\a_{p_y}\end{bmatrix},$$

$$[F]=\begin{bmatrix}k_{z,\nu_0}\int_{S_a}w_{s_x}e^h_{x,\nu_0}ds\\k_{z,\nu_0}\int_{S_a}w_{s_y}e^h_{y,\nu_0}ds\end{bmatrix}.$$

The Region B mode amplitude coefficients are then found by substituting the solution for $[X]$ into (3.1.3).

3.1.1 Basis and Weighting Functions

An important aspect of solving the aperture problem is the choice of the basis and weighting function sets. Choosing incorrectly may lead to poor convergence or an erroneous solution. The linear operator, L, in the inner product generally influences how the function sets are chosen. Function sets may be required to have a certain order of smoothness, depending on the form of L, such that the inner product terms remain well defined. One may also consider a function set that simplifies the evaluation of the inner product terms. One possibility is a set of independent piece-wise functions where each

function is defined over a unique sub-interval of the solution space. Another possibility is to choose a set of harmonic functions. In this case, the functions are defined over the entire solution space and are independent in an orthogonal sense.

In the aperture problem, L is the integral of the Green's function. The Green's function is formed in part from equating the tangential electric fields to the unknown magnetic current in the aperture and to zero on the iris. Since the tangential electric field is a modal form (harmonic basis), it would be appropriate to also represent the magnetic current basis as a set of harmonic functions. Although harmonic functions are orthogonal, they also satisfy the most important condition of linear independence. In addition, a simpler analysis and better convergence may be obtained if the basis functions satisfy the correct boundary conditions at the aperture boundary, that is

$$\begin{aligned} M_{s_x} &= 0, \qquad x = c_1,\ x = c_2 \\ M_{s_y} &= 0, \qquad y = v_1,\ y = v_2 \end{aligned}. \tag{3.1.6}$$

A harmonic basis set that satisfies these conditions is

$$\begin{aligned} u_{x,pq}(\vec{\rho}') &= \sin\Big(\frac{p\pi(x'-c_1)}{c}\Big)\cos\Big(\frac{q\pi(y'-v_1)}{v}\Big) \\ u_{y,pq}(\vec{\rho}') &= \cos\Big(\frac{p\pi(x'-c_1)}{c}\Big)\sin\Big(\frac{q\pi(y'-v_1)}{v}\Big), \end{aligned} \tag{3.1.7}$$

where $c_1 \le x \le c_2$ and $v_1 \le y \le v_2$. The subscript p has been replaced by the (p,q) designation. This essentially approximates the magnetic current as a half-range Fourier series defined over the aperture. We will choose the weighting functions as

$$\begin{aligned} w_{x,st}(\vec{\rho}) &= \cos\Big(\frac{s\pi(x-c_1)}{c}\Big)\sin\Big(\frac{t\pi(y-v_1)}{v}\Big) \\ w_{y,st}(\vec{\rho}) &= \sin\Big(\frac{s\pi(x-c_1)}{c}\Big)\cos\Big(\frac{t\pi(y-v_1)}{v}\Big). \end{aligned} \tag{3.1.8}$$

The number of aperture unknowns used in the x-dimension for both the basis and weighting functions is truncated at order P. In the y-dimension, the number of unknowns is truncated at order Q.

After substituting the basis and weighting functions into (3.1.5), we find that the matrix elements consist of only two integral forms. These are

$$\int_{c_1}^{c_2}\int_{v_1}^{v_2}\cos(\frac{p\pi x}{c})\sin(\frac{q\pi y}{v})\cos(\frac{m\pi x}{a})\sin(\frac{n\pi y}{b})dydx$$
$$\int_{c_1}^{c_2}\int_{v_1}^{v_2}\sin(\frac{p\pi x}{c})\cos(\frac{q\pi y}{v})\sin(\frac{m\pi x}{a})\cos(\frac{n\pi y}{b})dydx, \quad (3.1.9)$$

which can be evaluated analytically. A computer program, written in FORTRAN, fills the elements in the matrix equation given by (3.1.5). The matrix inversion and corresponding multiplication are performed by implementing LU decomposition and back substitution routines [21].

3.1.2 Verification

The purpose of this section is to determine the validity of the aperture solution and investigate its limitations. The computer program, written in FORTRAN, can compute the reflection coefficient for a variety of parameters outlined in Table 3.1. The convergence of the solution is dependent how the aperture and waveguide modes are truncated. As stated previously, P and Q are the orders of truncation for the aperture modes in the x and y-dimensions, respectively. The waveguide modes are truncated at orders M and N in the x and y-dimensions, respectively. That is, $m = 1, 2, \ldots, M$ and $n = 0, 1, \ldots, N-1$. For an inductive iris, where the width of the aperture varies in the x direction, the parameters M and P must be chosen correctly. Since the waveguide remains uniform in the y direction, only a single unknown is required for N and Q. Similarly, the parameters N and Q are important for a capacitive iris. For a capacitive iris, the width of the aperture varies in the y direction and the waveguide remains uniform in the x direction. The order of truncation for the waveguide modes determines how well the Green's function converges. How well the aperture magnetic current is approximated is determined by the number of aperture modes.

Table 3.1 Parameters for Aperture Program

$a =$ waveguide dimension in x
$b =$ waveguide dimension in y
$c =$ aperture dimension in x
$v =$ aperture dimension in y
$f =$ nominal frequency
P and $Q =$ number of aperture modes in x and y, respectively
M and $N =$ number of waveguide modes in x and y, respectively.

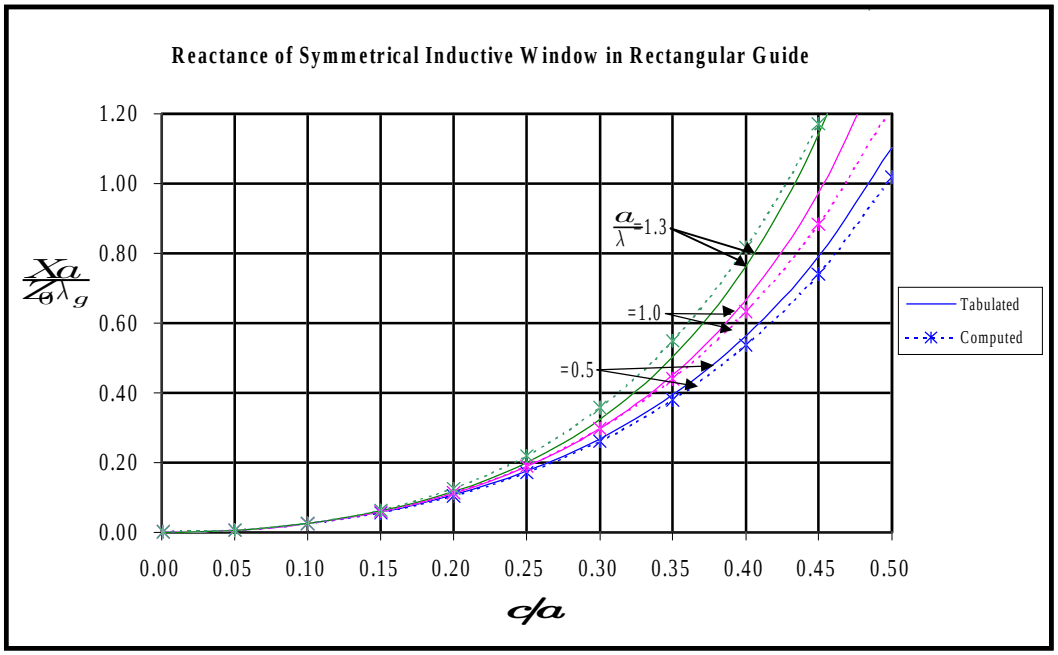

Fig. 3.1*a* Comparison of Computed and Tabulated Aperture Reactance

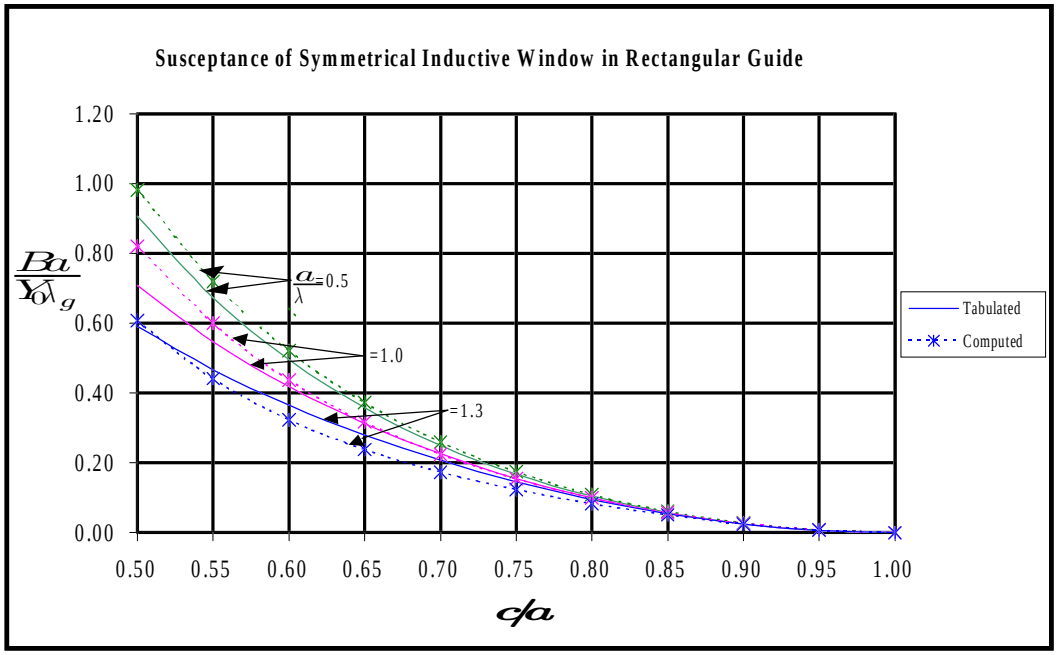

Fig. 3.1*b* Comparison of Computed and Tabulated Aperture Susceptance

To verify the Green's function approach to the aperture interface developed in Chapter 2, numerical results for the reactance and susceptance of a symmetrical inductive iris obtained from the computer program are compared to tabulated results [20]. Figure 3.1a compares the computed and tabulated values of the normalized reactance for various wavelengths and aperture widths in the range $0 < \frac{c}{a} < 0.5$. Figure 3.1b shows the computed and tabulated values for the normalized susceptance over the remaining aperture widths. The plots for the tabulated results were generated by programming the formulas given in [20]. It should be noted that the formula used for $0 < \frac{c}{a} < 0.5$ is valid for $\frac{c}{a} \ll 1$ and the formula used for $0.5 < \frac{c}{a} < 1$ is valid for $\frac{a-c}{2a} \ll 1$. The results compare well for a relatively few number of aperture unknowns.

The order of truncation is important to the convergence of the solution. The number of waveguide modes, denoted by M, determines how well the Green's function is approximated. The number of aperture unknowns, P, determines the convergence of the magnetic surface current. Furthermore, the ratio $\frac{M}{P}$ required for convergence of the solution depends on the width of the aperture. Figure 3.2 is a plot of the normalized aperture reactance versus the ratio of unknowns for a fixed aperture width. The solution converges very well if the unknowns are truncated approximately on the order of $M \geq P\frac{a}{c}$. Generally the wider the aperture, the more unknowns required in the aperture to approximate the magnetic surface current.

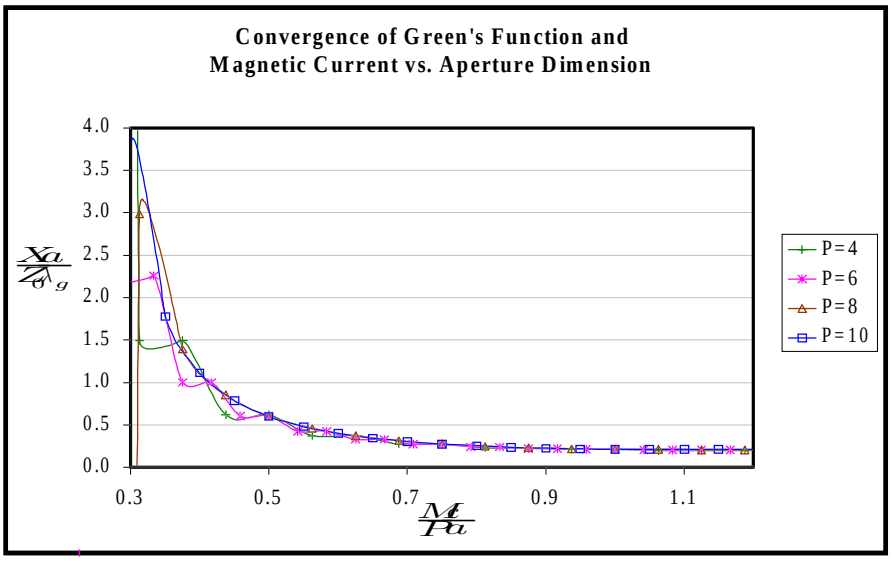

Fig. 3.2 Convergence of Green's Function and Magnetic Current

3.2 Fiber Solution

The fiber solution developed in Section 2.3.6 gives the reflected mode amplitude coefficients in terms of the incident mode amplitude coefficients for a fiber located in an open-ended rectangular waveguide. The complete mode structure has been included to investigate the possible effects of higher order modes incident on the fiber. However, if we assume that the fiber is located at a distance far from the source and that the waveguide supports only the dominant mode, we can simplify the general fiber solution to

$$\begin{bmatrix} B_{\nu}^{h(-)} \\ B_{\nu}^{e(-)} \end{bmatrix} = \begin{bmatrix} M_{1_{\nu 1}} \\ M_{3_{\nu 1}} \end{bmatrix} \begin{bmatrix} B_{\nu_0}^{h(+)} \\ B_{\nu_0}^{e(+)} \end{bmatrix}, \tag{3.2.1}$$

where $[M_{1_{\nu 1}}]$ and $[M_{3_{\nu 1}}]$ are the first rows of the matrix partitions $[M_1]$ and $[M_3]$, respectively, given in (2.3.6). This matrix equation allows us to determine the dominant mode reflection coefficient of the fiber for fields away from the fiber as well as the higher order modes required to determine the electric field profile along the fiber.

3.2.1 Verification

Similarly to the aperture solution, the validity of the fiber solution is investigated by comparing the computed reflection coefficient of the fiber to analytical results tabulated in [20]. A computer program implements the modal solution to determine the scattered modes from and incident TE_{10} mode field. The parameters for the computer program are outlined in Table 3.2.

Table 3.2 Parameters for Fiber Program

$a =$ waveguide dimension in x
$b =$ waveguide dimension in y
$t_a =$ diameter of fiber normalized to a
$\epsilon_{\mathrm{r}}'(y)$, $\epsilon_r''(y) =$ dielectric properties sampled along axis
$f =$ nominal frequency
$a_0 =$ location of fiber axis along x-axis
M and $N =$ number of waveguide modes in x and y, respectively.

The tabulated results consist of formulas for the normalized transmission line equivalent circuit parameters for a vertically orientated circular dielectric cylinder located in a TE_{10}-mode rectangular waveguide. Figure 3.3a compares the real part of the reflection coefficient obtained from the tabulated formulas to that obtained from the modal approach described in this thesis. The comparison is made over a range of values for the real dielectric constant for fibers of three different diameters. Similarly, Fig. 3.3b shows the imaginary part of the reflection coefficient. The accuracy of the modal approach is dependent on both the thickness of the fiber and the magnitude of the dielectric constant. As the diameter and the dielectric constant increase, the approximation begins to break down. A similar trend may be shown when the dielectric loss increases.

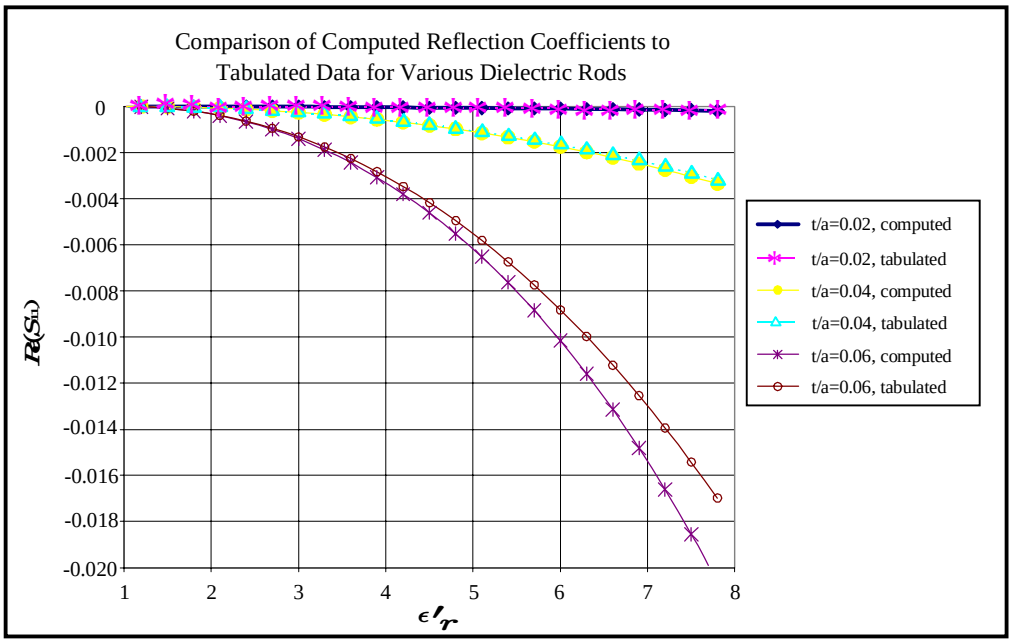

Fig. 3.3a Comparison of Computed and Tabulated Real Reflection Coefficient

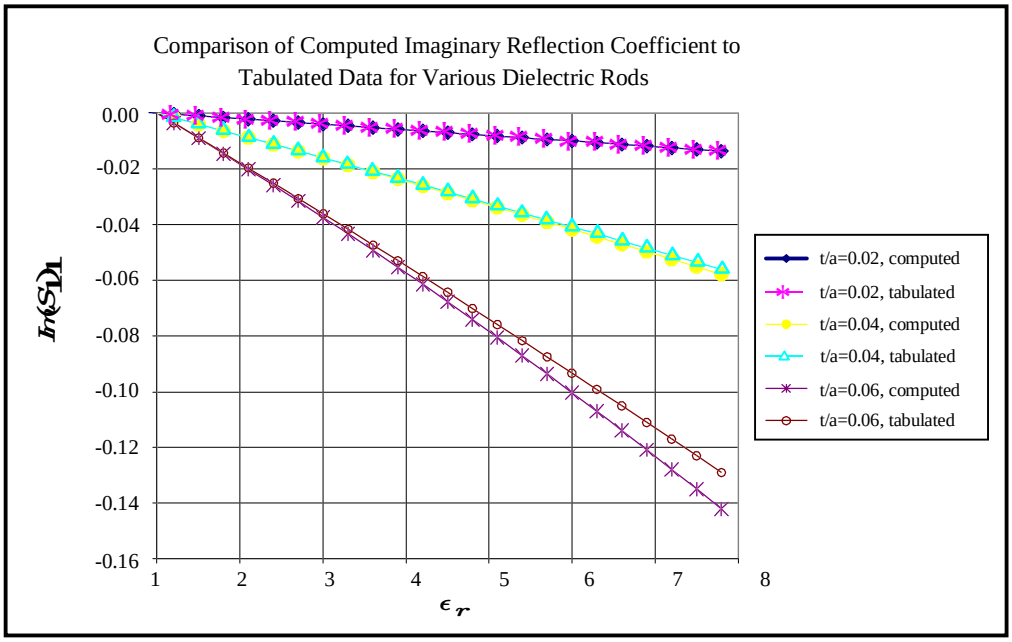

Fig. 3.3*b* Comparison of Computed and Tabulated Imaginary Reflection Coefficient

An important factor in the fiber solution is the choice of M and N, the truncation order of the waveguide modes in the x and y-dimensions, respectively. For a fiber with constant dielectric properties, only one waveguide mode is needed in the y-dimension. The integration of the conductivity term discussed in the previous section reduces to a constant. When the dielectric properties are a function of y, more unknowns are required to achieve a converged electric field profile along the fiber. In the x-dimension, the number of unknowns required is dependent on the diameter and permittivity of the fiber. Fewer unknowns may be used for a small diameter fiber with low permittivity than for a large diameter and high permittivity fiber.

3.2.2 Non-Uniform Heating

When the fiber undergoes non-uniform heating along its length, it becomes an inhomogeneous material due to the temperature-dependent dielectric constant. In this case, we must approximate the dielectric properties of the fiber. One way of

accomplishing this is to sample the relative permittivity at discrete points along the fiber, approximating the permittivity as piecewise constant. Sampling also provides a straightforward method of evaluating the expression

$$\int_0^b Y(y)\cos(\frac{n\pi y}{b})\cos(\frac{t\pi y}{b})dy \tag{2.3.82}$$

introduced in Section 2.3.6.

The finite difference solution of the heat conduction equation generates a temperature distribution at discrete points along the fiber. Using a subroutine to compute the dielectric properties for the temperature at each point, we obtain a discrete sampling of the conductivity along the fiber. If we represent the conductivity as a discrete exponential Fourier series, we can approximate (2.3.82) as a series of analytical integrals which can be evaluated in closed form. Given K sample points, the discrete exponential Fourier series of the conductivity term is

$$Y(k\Delta_y) = \sum_{l=-L}^{L-1} F_l e^{jl\frac{2\pi}{K}k}, \qquad \Delta_y = \frac{b}{K}. \tag{3.2.2}$$

The Fourier coefficients are given by

$$F_l = \frac{1}{K}\sum_{k=0}^{K-1} Y(k\Delta_y)e^{-j\frac{2\pi}{K}lk}. \tag{3.2.3}$$

Once the coefficients are determined using (3.2.3), we can approximate the conductivity as a continuous function of y as

$$Y(y) = \sum_{l=-L}^{L-1} F_l e^{jl\frac{2\pi}{b}y}. \tag{3.2.4}$$

This allows us to write (2.3.82) as a sum of analytical integrals. Expanding the product of cosine functions and substituting for the conductivity, we have

$$\frac{1}{2}\sum_{l=-L}^{L-1} F_l \int_0^b e^{jl\frac{2\pi}{b}y}\Big[\cos(\frac{\pi y(n+t)}{b}) + \cos(\frac{\pi y(n-t)}{b})\Big]dy. \tag{3.2.5}$$

Since $\cos(x)$ is an even function, we only need to evaluate

$$\Phi_i = \sum_{l=-L}^{L-1} F_l \int_0^b e^{jl\frac{2\pi}{b}y}\cos(\frac{i\pi y}{b})dy, \qquad i = 0, 1, \ldots, 2N, \tag{3.2.6}$$

where N is the total number of modes taken in y. An additional consideration is in choosing the number of Fourier coefficients and the number of sample points. To obtain a valid answer, these should be related to each other in a Nyquist sense as $K \geq 2L$ [22].

3.3 Complete Field Solution

The complete field solution involves combining the aperture and fiber solutions such that all of the modes from both interfaces couple together. To accomplish this, both the aperture and fiber solutions must be modified to include backward traveling modes. In this section, the formulation of the total solution is presented. The advantages and disadvantages in terms of the usefulness of incorporating all the modes is also discussed. Furthermore, the possibility of excluding the higher-order, evanescent modes to simplify the solution is introduced.

3.3.1 Modified Aperture Solution

In the modified aperture solution, the geometry of Region B is changed from an open-ended waveguide extending to infinity to a section of waveguide that terminates at the fiber interface. The transverse fields in this region now consist of both forward and backward traveling modes and are given as

$$\vec{E}_t^{\,B} = \sum_\nu \Big[\big(B_\nu^{h(+)} e^{-jk_{z,\nu}z} + B_\nu^{h(-)} e^{+jk_{z,\nu}(z-d_0)}\big)\vec{e}_{t,\nu}^{\,h} - \big(B_\nu^{e(+)} e^{-jk_{z,\nu}z} - B_\nu^{e(-)} e^{+jk_{z,\nu}(z-d_0)}\big)\vec{e}_{t,\nu}^{\,e} \Big] \tag{3.3.1a}$$

$$\vec{H}_t^{\,B} = -\sum_\nu \Big[\big(B_\nu^{h(+)} e^{-jk_{z,\nu}z} - B_\nu^{h(-)} e^{+jk_{z,\nu}(z-d_0)}\big)\vec{h}_{t,\nu}^{\,h} - \big(B_\nu^{e(+)} e^{-jk_{z,\nu}z} + B_\nu^{e(-)} e^{+jk_{z,\nu}(z-d_0)}\big)\vec{h}_{t,\nu}^{\,e} \Big]. \tag{3.3.1b}$$

Applying the continuity of the tangential electric fields over the waveguide cross-section at the aperture interface gives

$$\begin{aligned} A_\nu^h + \delta_{\nu\nu_0} &= B_\nu^{h(+)} + B_\nu^{h(-)} e^{-jk_{z,\nu}d_0} \\ A_\nu^e &= -B_\nu^{e(+)} + B_\nu^{e(-)} e^{-jk_{z,\nu}d_0}. \end{aligned} \tag{3.3.2}$$

In Section 2.3.2, we introduced a magnetic surface current defined in terms of the tangential electric field of Region A. The mode coefficients of Region A were then found in terms of the magnetic current using a Fourier analysis. Since the geometry of Region A is the same in the modified aperture solution, the expression

$$\begin{aligned} A_\nu^h + \delta_{\nu\nu_0} &= \sum_{p=1}^{P} \int_{S_a} \Big(- a_{p_x} u_{p_x} e_{y,\nu}^h + a_{p_y} u_{p_y} e_{x,\nu}^h \Big) ds \\ A_\nu^e &= \sum_{p=1}^{P} \int_{S_a} \Big(- a_{p_x} u_{p_x} e_{y,\nu}^e + a_{p_y} u_{p_y} e_{x,\nu}^e \Big) ds \end{aligned} \tag{3.1.1}$$

is still valid. Using (3.3.2) to relate the Region A and Region B coefficients, we can express (3.1.1) in matrix form as

$$\begin{bmatrix} B_\nu^{h(+)} \\ -B_\nu^{e(+)} \end{bmatrix} + \begin{bmatrix} B_\nu^{h(-)} e^{-jk_{z,\nu}d_0} \\ B_\nu^{e(-)} e^{-jk_{z,\nu}d_0} \end{bmatrix} = \begin{bmatrix} -\int_{S_a} u_{p_x} e_{y,\nu}^h ds & \int_{S_a} u_{p_y} e_{x,\nu}^h ds \\ -\int_{S_a} u_{p_x} e_{y,\nu}^e ds & \int_{S_a} u_{p_y} e_{x,\nu}^e ds \end{bmatrix} \begin{bmatrix} a_{p_x} \\ a_{p_y} \end{bmatrix}. \tag{3.3.3}$$

The remaining boundary condition required at the aperture is (2.3.50), the continuity of the tangential magnetic field in the aperture. The fields for the modified aperture solution are

$$\begin{aligned} \hat{z} \times \vec{H}_t^B &= \sum_\nu \Big[- \frac{1}{Z_\nu^h} \big(B_\nu^{h(+)} - B_\nu^{h(-)} e^{-jk_{z,\nu}d_0} \big) \vec{e}_{t,\nu}^h \\ &\qquad + \frac{1}{Z_\nu^e} \big(B_\nu^{e(+)} + B_\nu^{e(-)} e^{-jk_{z,\nu}d_0} \big) \vec{e}_{t,\nu}^e \Big] \\ \hat{z} \times \vec{H}_t^A &= \sum_\nu \Big[\frac{1}{Z_\nu^h} \big(B_\nu^{h(+)} + B_\nu^{h(-)} e^{-jk_{z,\nu}d_0} - 2\delta_{\nu\nu_0} \big) \vec{e}_{t,\nu}^h \\ &\qquad - \frac{1}{Z_\nu^e} \big(B_\nu^{e(+)} - B_\nu^{e(-)} e^{-jk_{z,\nu}d_0} \big) \vec{e}_{t,\nu}^e \Big]. \end{aligned} \tag{3.3.4}$$

Therefore, substituting (3.3.4) into (2.3.50) gives

$$\sum_\nu \Big[k_{z,\nu} B_\nu^{h(+)} \vec{e}_{t,\nu}^h - \frac{k^2}{k_{z,\nu}} B_\nu^{e(+)} \vec{e}_{t,\nu}^e \Big] = k_{z,\nu_0} \vec{e}_{t,\nu_0}^h, \qquad \text{in aperture.} \tag{3.3.5}$$

Applying the weighting functions to (3.3.5) as in Section 3.1 results in the matrix equation

$$\begin{bmatrix} k_{z,\nu} \int_{S_a} w_{s_x} e_{x,\nu}^h ds & -\frac{k^2}{k_{z,\nu}} \int_{S_a} w_{s_x} e_{x,\nu}^e ds \\ k_{z,\nu} \int_{S_a} w_{s_y} e_{y,\nu}^h ds & -\frac{k^2}{k_{z,\nu}} \int_{S_a} w_{s_y} e_{y,\nu}^e ds \end{bmatrix} \begin{bmatrix} B_\nu^{h(+)} \\ B_\nu^{e(+)} \end{bmatrix} = \begin{bmatrix} k_{z,\nu_0} \int_{S_a} w_{s_x} e_{x,\nu_0}^h ds \\ k_{z,\nu_0} \int_{S_a} w_{s_y} e_{y,\nu_0}^h ds \end{bmatrix}, \tag{3.3.6}$$

where $s = 1, 2, \ldots, P$. Following the same procedure developed in Section 3.1 would suggest that we substitute (3.3.3) for the Region B coefficients in (3.3.6). However, we

must first eliminate the $B_\nu^{(-)}$ coefficients from (3.3.3) to obtain an equation only in terms of the $B_\nu^{(+)}$ coefficients. We can accomplish this by using the relationship between $B_\nu^{(+)}$ and $B_\nu^{(-)}$ obtained from the fiber solution.

3.3.2 Modified Fiber Solution

The geometry for the fiber solution is modified to include the effects of the shorting plane as shown in Fig. 3.4. The modal solution form for the transverse fields in Region C are now of the cavity type. From Table 2.1, these are given as

$$\vec{E}_t^C = \sum_\nu \Big[\big(C_\nu^h \vec{e}_{t,\nu}^h + jC_\nu^e \vec{e}_{t,\nu}^e \big) \sin\big[k_{z,\nu}(z-d)\big] \Big] \tag{3.3.7a}$$

$$\vec{H}_t^C = -\sum_\nu \Big[\big(jC_\nu^h \vec{h}_{t,\nu}^h - C_\nu^e \vec{h}_{t,\nu}^e \big) \cos\big[k_{z,\nu}(z-d)\big] \Big], \tag{3.3.7b}$$

Enforcing the continuity of the tangential electric field over the waveguide cross-section at the fiber interface gives

$$\begin{aligned} C_\nu^h &= \frac{1}{\sin\big[k_{z,\nu}(d_0-d)\big]} \big(B_\nu^{h(+)} e^{-jk_{z,\nu}d_0} + B_\nu^{h(-)} \big) \\ C_\nu^e &= \frac{j}{\sin\big[k_{z,\nu}(d_0-d)\big]} \big(B_\nu^{e(+)} e^{-jk_{z,\nu}d_0} - B_\nu^{e(-)} \big). \end{aligned} \tag{3.3.8}$$

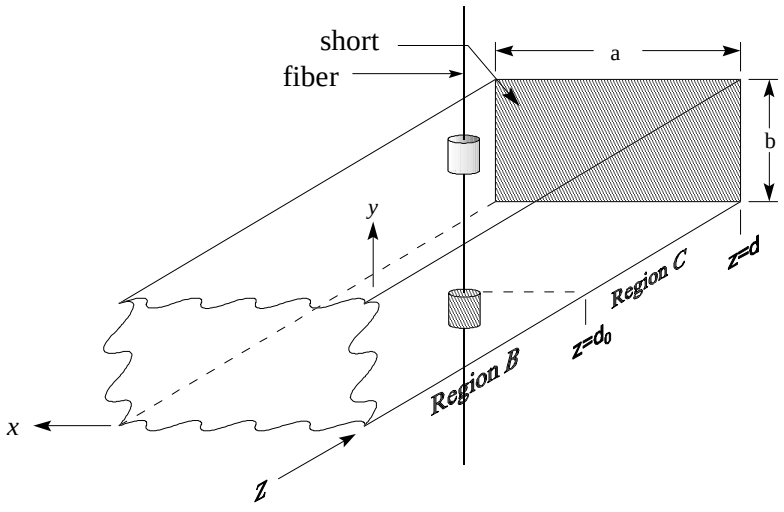

Fig. 3.4 Fiber Interface Including Short

As with the straight fiber solution, we use the boundary condition on the tangential magnetic fields at the fiber interface to ultimately relate the backward traveling modes to the forward traveling modes incident on the fiber. We substitute the modal solutions into (2.3.69) using (3.3.8) to obtain

$$\begin{aligned}\vec{J}_s = \hat{z}\times\left(\vec{H}^C-\vec{H}^B\right) = \sum_\nu\Bigg\{ &\frac{\vec{e}^{\,h}_{t,\nu}}{Z^h_\nu}\Big[B^{h(+)}_\nu\left(1-j\cot\left[k_{z,\nu}\left(d_0-d\right)\right]\right)e^{-jk_{z,\nu}d_0}\\ &\qquad -B^{h(-)}_\nu\left(1+j\cot\left[k_{z,\nu}\left(d_0-d\right)\right]\right)\Big]\\ &-\frac{\vec{e}^{\,e}_{t,\nu}}{Z^e_\nu}\Big[B^{e(+)}_\nu\left(1-j\cot\left[k_{z,\nu}\left(d_0-d\right)\right]\right)e^{-jk_{z,\nu}d_0}\\ &\qquad +B^{e(-)}_\nu\left(1+j\cot\left[k_{z,\nu}\left(d_0-d\right)\right]\right)\Big]\Bigg\}.\end{aligned} \tag{3.3.9}$$

Similar to the straight fiber solution, we define the coefficients

$$\begin{aligned}H^h_\nu &= \frac{1}{Z^h_\nu}\Big[B^{h(+)}_\nu\left(1-j\cot\left[k_{z,\nu}\left(d_0-d\right)\right]\right)e^{-jk_{z,\nu}d_0}\\ &\qquad -B^{h(-)}_\nu\left(1+j\cot\left[k_{z,\nu}\left(d_0-d\right)\right]\right)\Big]\\ H^e_\nu &= -\frac{1}{Z^e_\nu}\Big[B^{e(+)}_\nu\left(1-j\cot\left[k_{z,\nu}\left(d_0-d\right)\right]\right)e^{-jk_{z,\nu}d_0}\\ &\qquad +B^{e(-)}_\nu\left(1+j\cot\left[k_{z,\nu}\left(d_0-d\right)\right]\right)\Big],\end{aligned} \tag{3.3.10}$$

where the equations

$$\begin{aligned}H^h_\nu &= \int_{S_w}\left[e^h_{y,\nu}E^B_{0y}YA_f\delta\left(x-a_0\right)\right]ds\\ H^e_\nu &= \int_{S_w}\left[e^e_{y,\nu}E^B_{0y}YA_f\delta\left(x-a_0\right)\right]ds\end{aligned} \tag{2.3.83}$$

obtained from the Fourier analysis remain unchanged. The difference between the modified fiber solution becomes apparent when we equate (2.3.83) and (3.3.10) to obtain

$$\begin{aligned}&\left[B^{h(+)}_\nu\left(1-j\cot\left[k_{z,\nu}\left(d_0-d\right)\right]\right)e^{-jk_{z,\nu}d_0}-B^{h(-)}_\nu\left(1+j\cot\left[k_{z,\nu}\left(d_0-d\right)\right]\right)\right]\\ &\quad = Z^h_\nu\int_{S_w}\Big[YA_f\delta\left(x-a_0\right)e^h_{y,\nu}\sum_\gamma\Big\{e^h_{0y,\gamma}\left(B^{h(+)}_\gamma e^{-jk_{z,\gamma}d_0}+B^{h(-)}_\gamma\right)\\ &\qquad\qquad -e^e_{0y,\gamma}\left(B^{e(+)}_\gamma e^{-jk_{z,\gamma}d_0}-B^{e(-)}_\gamma\right)\Big\}\Big]ds\end{aligned} \tag{3.3.11a}$$

and

$$\begin{aligned}\Big[B_\nu^{e(+)}\big(1-j\cot\big[k_{z,\nu}\big(d_0-d\big)\big]\big)e^{-jk_{z,\nu}d_0}+B_\nu^{e(-)}\big(1+j\cot\big[k_{z,\nu}\big(d_0-d\big)\big]\big)\Big]\\ =\ -Z_\nu^e\int_{S_w}\Big[YA_f\delta\big(x-a_0\big)e_{y,\nu}^e\sum_\gamma\Big\{e_{0y,\gamma}^h\big(B_\gamma^{h(+)}e^{-jk_{z,\gamma}d_0}+B_\gamma^{h(-)}\big)\\ -e_{0y,\gamma}^e\big(B_\gamma^{e(+)}e^{-jk_{z,\gamma}d_0}-B_\gamma^{e(-)}\big)\Big\}\Big]ds,\end{aligned}\tag{3.3.11b}$$

which is a set of $2\mathcal{N}$ equations with $4\mathcal{N}$ unknowns. The left hand side of these equations now contains coefficients for the forward traveling modes. The effects of the shorting plane are seen by the appearance of the co-tangent term. The elements of the partitioned matrix equation $[0]=[M^{(+)}][B^{(+)}]+[M^{(-)}][B^{(-)}]$ are exactly the same as derived in the straight fiber solution except that the diagonal elements include the cavity behavior for both the forward and backward traveling modes.

$$\begin{aligned}M_{1,\nu\gamma}^{(+)}&=\ -Z_\nu^h\mathcal{I}_{\nu\gamma}^{hh}e^{-jk_{z,\gamma}d_0}+\delta_{\nu\gamma}\big(1-j\cot\big[k_{z,\nu}\big(d_0-d\big)\big]\big)e^{-jk_{z,\nu}d_0}\\ M_{2,\nu\gamma}^{(+)}&=Z_\nu^h\mathcal{I}_{\nu\gamma}^{he}e^{-jk_{z,\gamma}d_0}\\ M_{3,\nu\gamma}^{(+)}&=Z_\nu^e\mathcal{I}_{\nu\gamma}^{eh}e^{-jk_{z,\gamma}d_0}\\ M_{4,\nu\gamma}^{(+)}&=\ -Z_\nu^e\mathcal{I}_{\nu\gamma}^{ee}e^{-jk_{z,\gamma}d_0}+\delta_{\nu\gamma}\big(1-j\cot\big[k_{z,\nu}\big(d_0-d\big)\big]\big)e^{-jk_{z,\nu}d_0}\\ M_{1,\nu\gamma}^{(-)}&=\ -Z_\nu^h\mathcal{I}_{\nu\gamma}^{hh}-\delta_{\nu\gamma}\big(1+j\cot\big[k_{z,\nu}\big(d_0-d\big)\big]\big)\\ M_{2,\nu\gamma}^{(-)}&=\ -Z_\nu^h\mathcal{I}_{\nu\gamma}^{he}\\ M_{3,\nu\gamma}^{(-)}&=Z_\nu^e\mathcal{I}_{\nu\gamma}^{eh}\\ M_{4,\nu\gamma}^{(-)}&=Z_\nu^e\mathcal{I}_{\nu\gamma}^{ee}+\delta_{\nu\gamma}\big(1+j\cot\big[k_{z,\nu}\big(d_0-d\big)\big]\big)\\ \mathcal{I}_{\nu\gamma}^{\substack{h\,h\\e\,e}}&=A_f\int_{S_w}\overset{h}{e}{}_{y,\nu}^{e}\overset{h}{e}{}_{0y,\gamma}^{e}Y\big(y\big)\delta\big(x-a_0\big)ds\end{aligned}\tag{3.3.12}$$

Once the matrix elements are computed, the coefficients for the backward traveling modes may be determined in terms of the coefficients for the forward traveling modes through a matrix inversion.

3.3.3 Combined Fiber and Aperture Problems

The fiber solution developed in Section 2.3.6 and modified in Section 3.3.2 allows us to express the coefficients for the backward traveling modes in terms the coefficients for the forward traveling modes through a matrix relation given as

$$\big[B^{(-)}\big] = \big[M\big]\big[B^{(+)}\big]. \tag{2.3.78}$$

Let us write (3.3.3) from the modified aperture solution as

$$\begin{bmatrix} I & 0 \\ 0 & -I \end{bmatrix}\begin{bmatrix} B_\nu^{h(+)} \\ B_\nu^{e(+)} \end{bmatrix} + \begin{bmatrix} \delta_{\nu\gamma}e^{-jk_{z,\nu}d_0} & 0 \\ 0 & \delta_{\nu\gamma}e^{-jk_{z,\nu}d_0} \end{bmatrix}\begin{bmatrix} B_\nu^{h(-)} \\ B_\nu^{e(-)} \end{bmatrix} = \begin{bmatrix} D_1 & D_2 \\ D_3 & D_4 \end{bmatrix}\begin{bmatrix} a_{p_x} \\ a_{p_y} \end{bmatrix}, \tag{3.3.13}$$

where ν and γ are the row and column indices, respectively, truncated at order $\nu = \gamma = \mathcal{N}$. The matrix $\big[I\big]$ is the $\mathcal{N}\times\mathcal{N}$ dimension identity matrix, $\big[D\big]$ is the partitioned integral matrix in (3.3.3), and

$$\big[\delta_{\nu\gamma}e^{-jk_{z,\nu}d_0}\big] = \begin{bmatrix} e^{-jk_{z,1}d_0} & 0 & 0 & \cdots & 0 \\ 0 & e^{-jk_{z,2}d_0} & 0 & \cdots & 0 \\ \vdots & \vdots & \ddots & & \vdots \\ 0 & 0 & 0 & \cdots & e^{-jk_{z,(\mathcal{N})}d_0} \end{bmatrix}.$$

Upon substituting (2.3.78) for the $B^{(-)}$ coefficients, (3.3.13) becomes

$$\begin{bmatrix} T_1 & T_2 \\ T_3 & T_4 \end{bmatrix}\begin{bmatrix} B_\nu^{h(+)} \\ B_\nu^{e(+)} \end{bmatrix} = \begin{bmatrix} D_1 & D_2 \\ D_3 & D_4 \end{bmatrix}\begin{bmatrix} a_{p_x} \\ a_{p_y} \end{bmatrix}, \tag{3.3.14}$$

where

$$\begin{bmatrix} T_1 & T_2 \\ T_3 & T_4 \end{bmatrix} = \begin{bmatrix} I & 0 \\ 0 & -I \end{bmatrix} + \begin{bmatrix} \delta_{\nu\gamma}e^{-jk_{z,\nu}d_0} & 0 \\ 0 & \delta_{\nu\gamma}e^{-jk_{z,\nu}d_0} \end{bmatrix}\begin{bmatrix} M_1 & M_2 \\ M_3 & M_4 \end{bmatrix}.$$

Following a matrix inversion of $\big[T\big]$, we obtain

$$\big[B^{(+)}\big] = \big[T\big]^{-1}\big[D\big]\big[a\big], \tag{3.3.15}$$

which is substituted into (3.3.6). The remainder of the problem is solved similarly to the general aperture problem by solving for the $\big[a\big]$ coefficients. The $\big[B^{(+)}\big]$ coefficients are then found from (3.3.15). The $\big[B^{(-)}\big]$ coefficients are computed using the fiber relation (2.3.78).

3.3.4 Field Distribution Results

Uniform Heating

The effects of the field interaction with the fiber are depicted through various plots of the magnitude of the y-component of the electric field. This component is the main focus since the waveguide and cavity support only the dominant TE_{10} mode. Also, the electric field tangential to the fiber is the quantity of interest to the heat transfer solution. The electric field distribution for a TE_{102} cavity and an aperture width $\frac{c}{a} = 0.1$ is shown in Fig. 3.5. The length of the cavity is $d = \lambda_g$ and the fiber is located at the second resonant peak $d_0 = \frac{3\lambda_g}{4}$. The small peak in the electric field strength at $z = d_0$ is a result of the fiber interaction. This type of field distribution is consistent with Rayleigh scattering from a dielectric obstacle. Lanz [23] obtained a similar peak in the field distribution when solving the microwave field interaction with a dielectric material falling into the Rayleigh scattering range. The field distribution in the vicinity of the coupling aperture suggests that the aperture effects do not penetrate into the cavity. From this fact we conclude that the full coupling of higher order modes between the aperture and the fiber is not necessary. In a multi-mode applicator configuration, this solution would still be required to provide a method for determining multi-mode interactions.

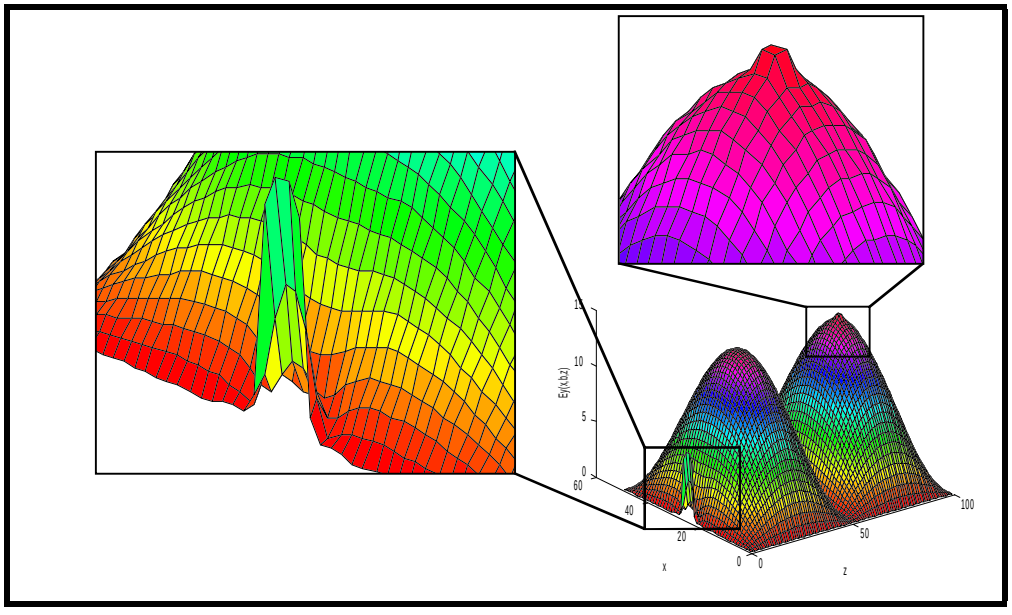

Fig. 3.5 E_y Distribution in Cavity for the $y = b$ Plane

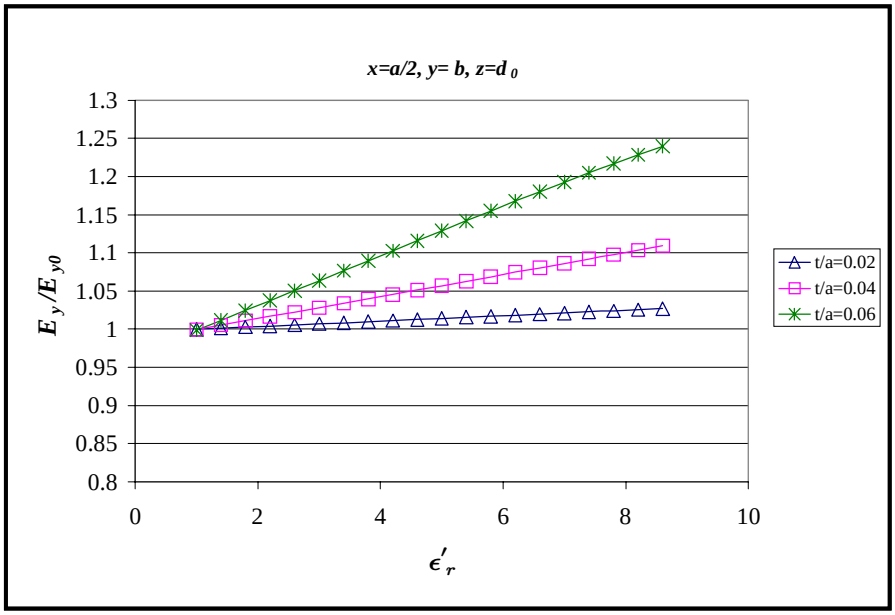

Fig. 3.6 Peak Electric Field Increase at Fiber vs. Dielectric Constant and Fiber Diameter

The heat transfer solution depends on both the value of the dielectric loss and the strength of the electric field component tangential to the fiber. Figure 3.6 depicts the level of peaking in the electric field at the fiber versus the dielectric constant for various diameters. The y-axis is a measure of the electric field strength at the fiber normalized to the electric field strength at the other peak, that is at $z = \frac{\lambda_g}{4}$. The electric field strength is strongly dependent on the fiber parameters. The peaking increases for fibers of increasing diameter and dielectric constant. This behavior may be important in determining how much increase in field strength to expect from a given increase in temperature. The main conclusion drawn from this plot is that the temperature dependent nature of the dielectric constant impacts the heat conduction equation indirectly by affecting the electric field strength at the fiber.

Another effect of the field interaction with the fiber is the shift in resonant frequency. The lowering of the resonant frequency of the cavity is seen in Fig. 3.7 which depicts the y-component of the electric field versus z, the longitudinal position in the

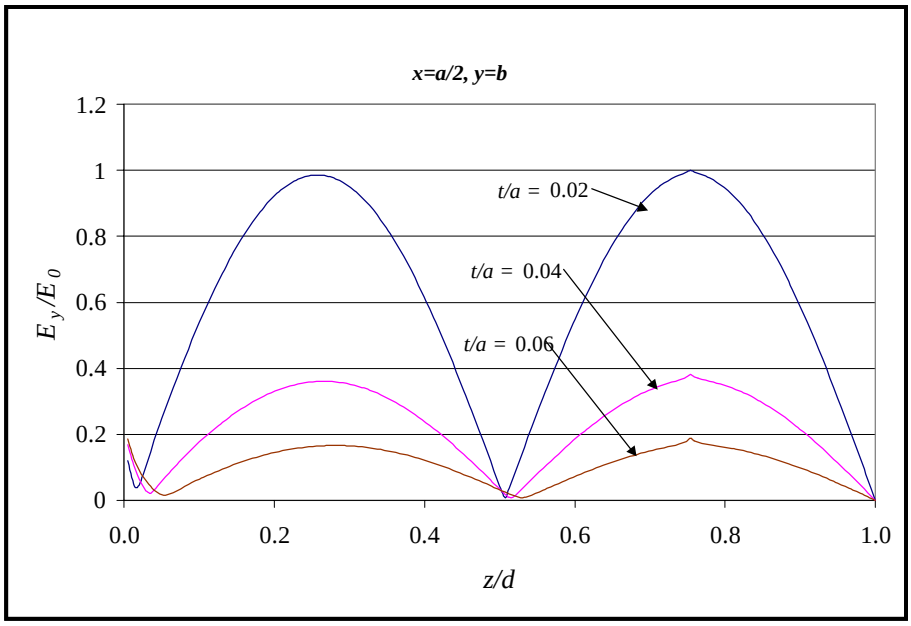

Fig. 3.7 Cavity Detuning Effects for Various Fibers

cavity. The electric field is normalized to the peak value at the fiber for the $\frac{t}{a} = 0.02$ case. The detuning effect increases with the diameter and dielectric constant of the fiber. The loss in the fiber also affects the overall field strength. When the length of the cavity was re-adjusted for maximum field strength, it was found that this new maximum was still lower than the initial field. This is most likely due to the effects of the dielectric loss absorbing the additional power from the system.

The amount of power absorbed in the fiber depends on the dielectric loss and the electric field strength along the fiber. When the fiber heats initially, its temperature and corresponding loss factor are low. Figure 3.8 shows the strength of the electric field along the fiber versus temperature to maintain a constant power absorbed of 20 watts. The diameter of the fiber is 2mm and the temperature dependent dielectric properties of Fig. 2.7 have been used. The electric field was computed from the computer program using a uniform temperature distribution, and hence a uniform permittivity distribution along the fiber. To achieve a constant level of power absorption, the electric field must initially have

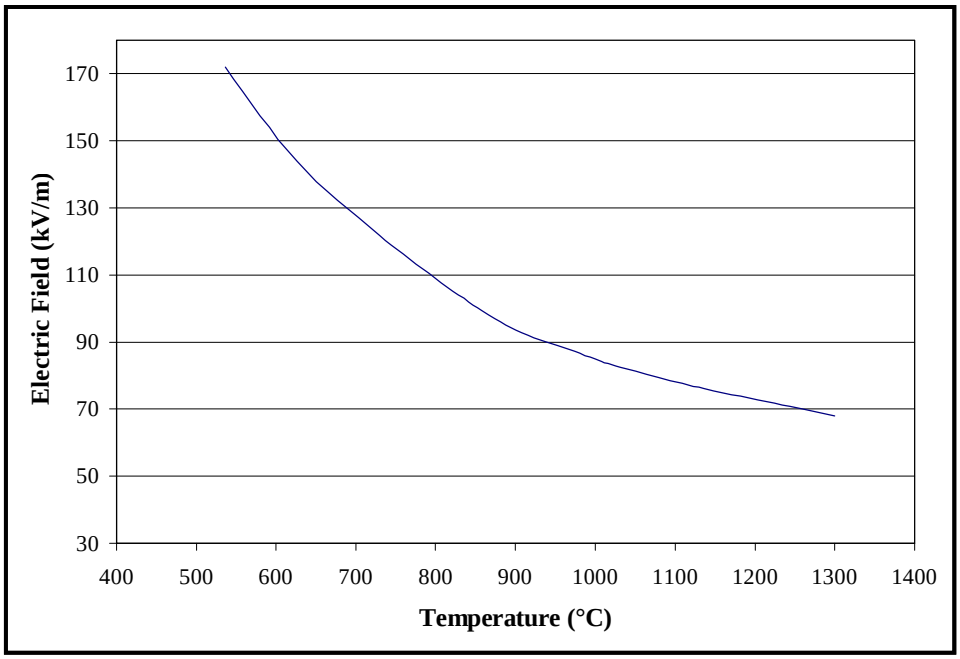

Fig. 3.8 Electric Field Strength vs. Temperature for 20W Constant Absorbed Power for a 2mm Ceramic Rod

a large magnitude. As the temperature and corresponding loss of the fiber increase, the electric field decreases.

The relationship between the absorbed power, electric field strength, and the dielectric loss may be shown explicitly through the definition of absorbed power obtained through a heat transfer analysis [3]. The definition for absorbed power is given by

$$P_{abs} = \int_{V_f} \dot{q}\, dv = \int_{V_f} \left(2\pi f \epsilon_0 \epsilon_r'' |E_y|^2\right) dv, \tag{3.3.16}$$

where V_f is the volume of the fiber. We can see from this equation that for a constant power the electric field and dielectric loss must vary as

$$|E_y| \sim \frac{1}{\sqrt{\epsilon_r''}}. \tag{3.3.17}$$

A comparison of this relationship obtained from the thermal approach and electromagnetic solution is shown in Fig. 3.9. The upper curve is the same given in Fig. 3.8 for the electromagnetic solution and the lower curve is obtained from (3.3.16). The relationship

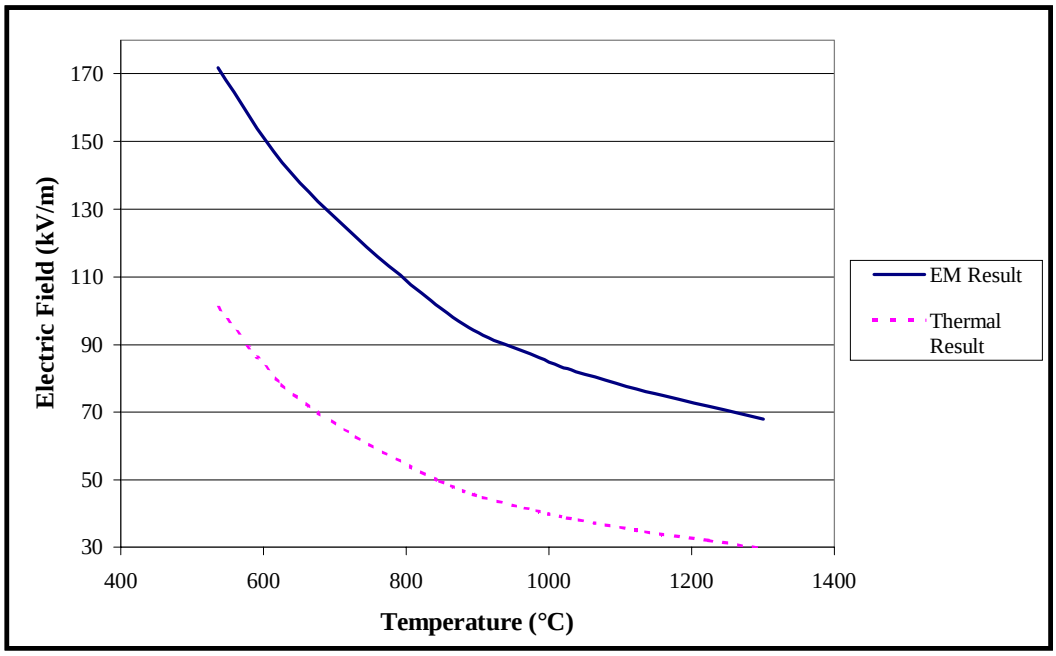

Fig. 3.9 Comparison of Electric Field vs. Temperature Relationships for Electromagnetic and Thermal Results

trends for both solutions compare well given the same set of parameters. Figure 3.9 shows that the electric field, computed from the simulation presented in this thesis, versus temperature for constant absorbed power does exhibit the correct relationship of (3.3.17).

Non-Uniform Heating

The effects of a non-uniform temperature distribution are investigated by specifying a sampled profile of the temperature-dependent complex permittivity along the fiber. The two heating situations explored in this section are models of the continuous and stationary processing experiments performed at the Los Alamos National Laboratory (LANL). The temperature distribution depicted in Fig. 3.10*a* shows the hot spot formation centered at the mid-point of the fiber. Figure 3.11*a* is the temperature distribution obtained during a simulation of continuous processing [3]. In this latter case,

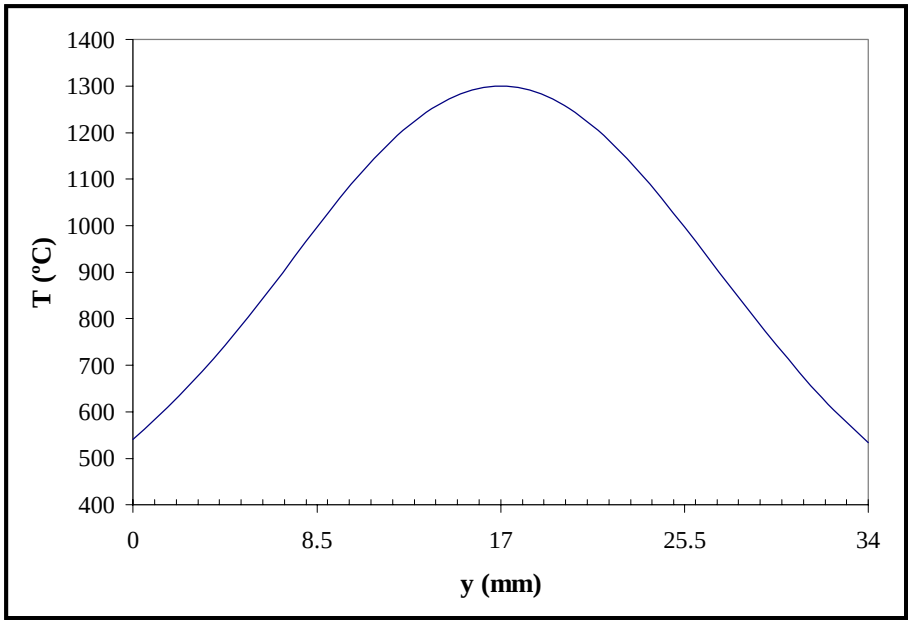

Fig. 3.10*a* Temperature Profile for Stationary Heating [4]

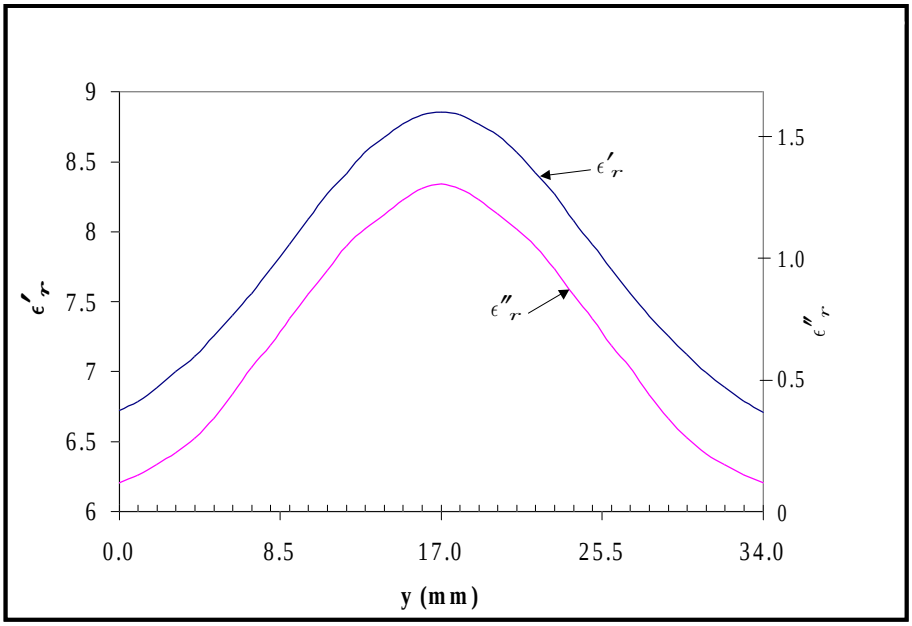

Fig. 3.10*b* Relative Permittivity of Fiber for Non-Uniform Stationary Heating

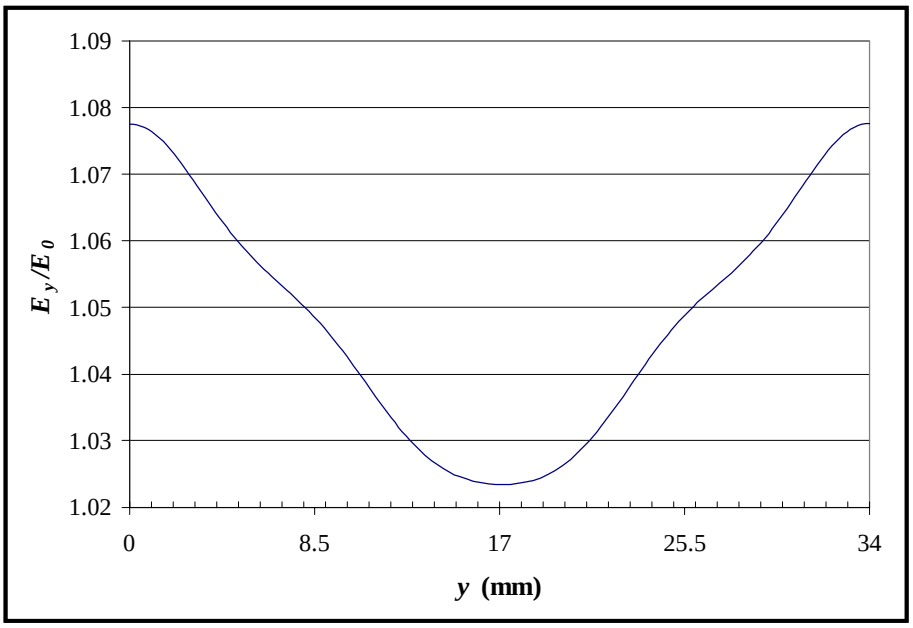

Fig. 3.10*c* Electric Field Profile Along Fiber for Stationary Heating

the hot spot drifts in the direction of the fiber velocity through the cavity. In both of these models, uniform electric field profiles were assumed in the solution to the heat conduction equation.

To generate the complex permittivity samples, the permittivity as a function of temperature and the desired temperature distribution as a function of position were entered into a spreadsheet. From these data, the dielectric properties could be found at any position along the fiber using a polynomial curve fit interpolation. Figs. 3.10(*a*-*c*) show the effects of non-uniform heating during stationary processing. The temperature distribution used and the corresponding interpolated dielectric properties along the fiber are shown in Fig. 3.10*a* and Fig. 3.10*b*, respectively. The increase in permittivity correlates to a decrease in the electric field strength along the fiber, as shown in Fig. 3.10*c*. Similarly, Figs. 3.11(*a*-*c*) depict the material and field variations for a hot spot shifted toward the exit end of the fiber. This helps to verify the trend of the electric field-permittivity relationship. Further investigation is required into the heat transfer analysis to determine whether this field variation has an impact on the heating of the fiber.

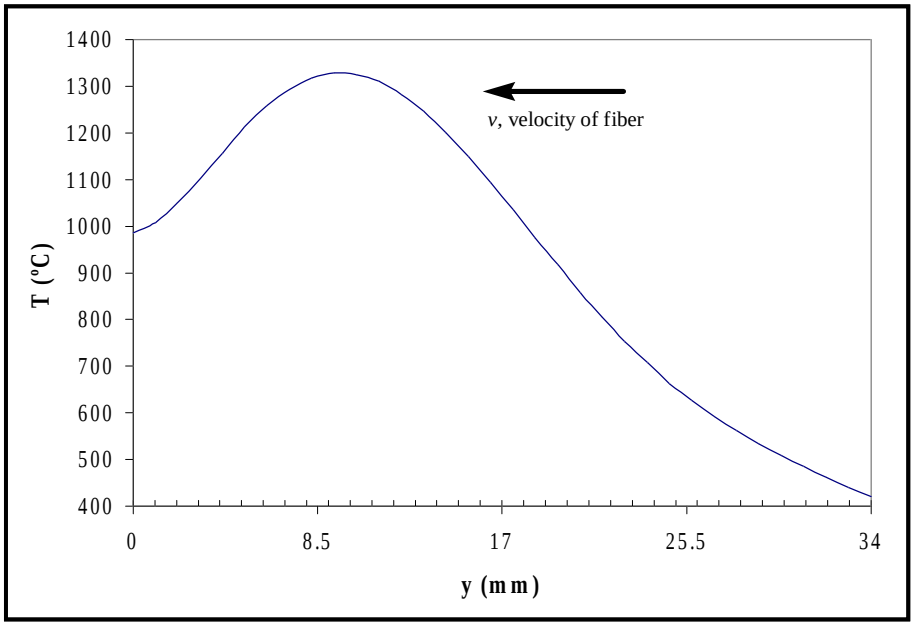

Fig. 3.11*a* Temperature Profile for Continuous Heating [4]

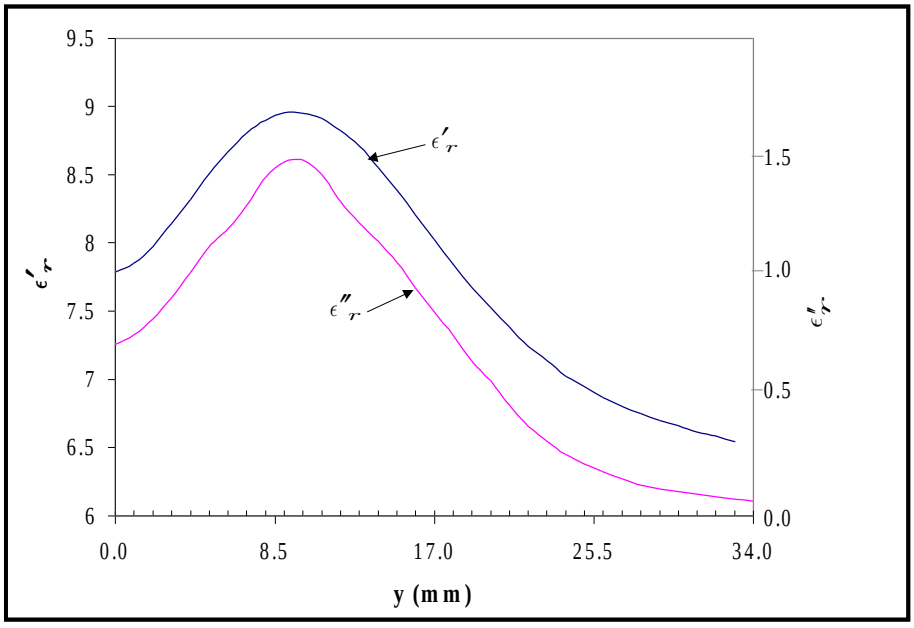

Fig. 3.11*b* Relative Permittivity of Fiber for Non-Uniform Continuous Heating

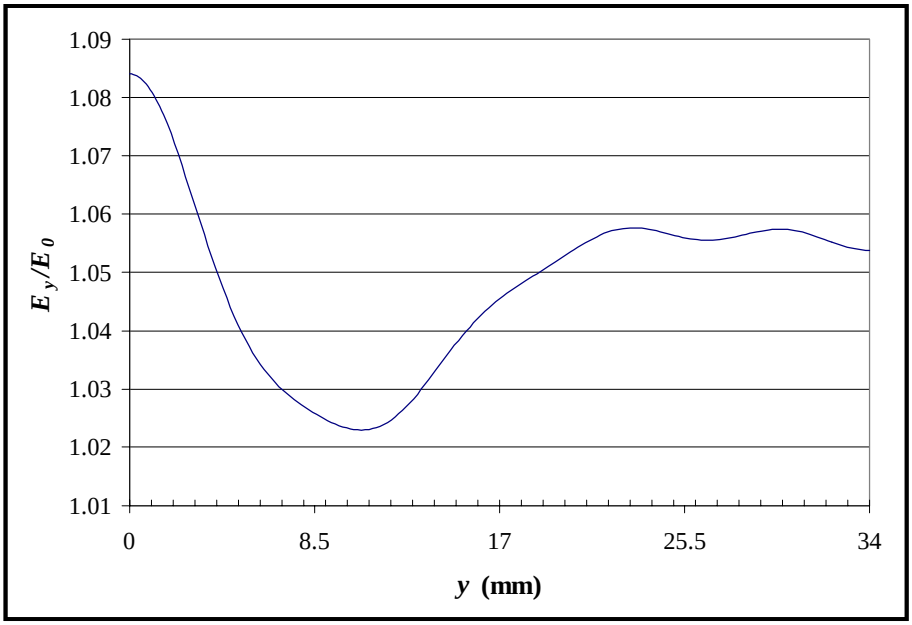

Fig. 3.11*c* Electric Field Profile Along Fiber for Continuous Heating

The overall impact of the fiber on the electric field distribution can be seen by plotting the field distribution along the fiber versus distance away from the fiber. Figure 3.12 is a plot of the y-component of the electric field in the $x = \frac{a}{2}$ plane. This shows that only the dominant TE_{10} mode propagates away from the fiber. The electric field distribution for the TE_{10} mode is constant in an unloaded cavity. The inhomogeneous fiber, in this case for the continuous processing temperature distribution, essentially creates a slight perturbation in the otherwise uniform field. We can conclude that the higher order modes are required to evaluate this effect in the vicinity of the fiber. Away from the fiber, we only require the dominant-mode coefficient.

An additional consideration is in the choice of the number of waveguide modes to use in the x and y dimensions. Relatively few unknowns in the y-dimension were required to converge to the distribution shape of the electric field. However, if too few unknowns were taken in the x-dimension, oscillations in the distribution became very apparent. The number of modes in x is important to the convergence of the magnitude of the field variations. The number of modes in y is more important to the convergence of the distribution shape.

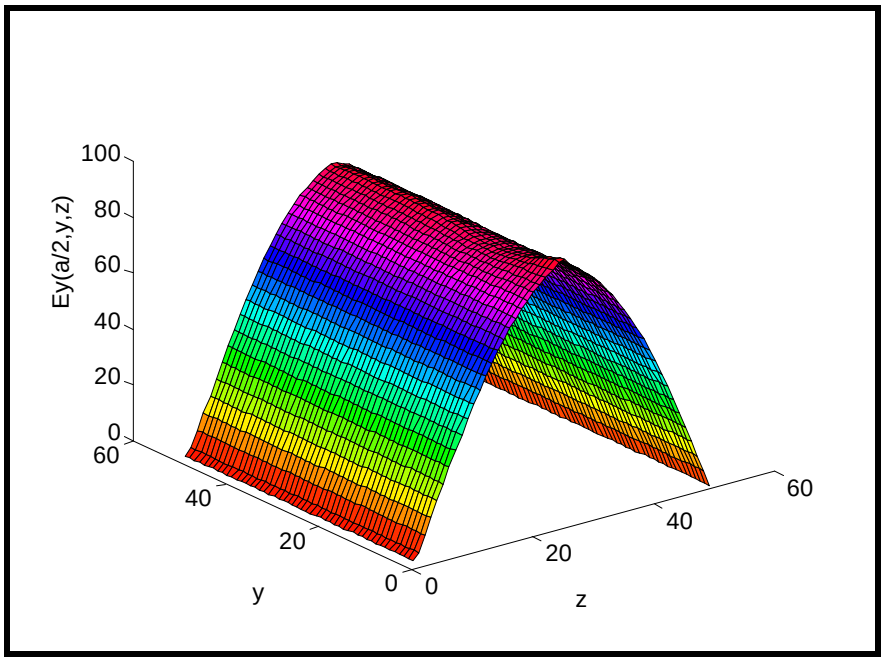

Fig. 3.12 E_y Distribution in Cavity for the $x = a/2$ Plane

3.3.5 Restricted Mode Solution

A restricted mode solution may reduce the complexity of the problem by saving computation time without adversely affecting the results. Since the higher order modes generated by the coupling aperture do not couple into the fiber, as seen from the results in the previous section, it is not necessary to include them in the complete solution. The aperture interaction may essentially be removed from the analysis using scattering matrix theory, as presented by Hile et al. [12]. An S-parameter format may be used to model the transmission and reflection characteristics of the dominant, propagating mode with the aperture as found in Section 3.1. The mode-matching solution to the field interaction with the fiber may be used compute the higher-order mode effects in the vicinity of the fiber to complete the problem. This approach is recommended for future work.

4. Conclusion

4.1 Summary

The microwave heating of ceramic fibers offers a number of advantages over conventional processing. However, phenomena such as thermal runaway and non-uniform heating are problems that currently limit the use of microwave processing on a large scale. An accurate understanding of the heating process through experiments and numerical simulation is vital to improving current methods. The research presented in this paper investigated the potential field distribution effects caused by shaping the coupling aperture, the effects of the temperature-dependent dielectric properties on the field distribution, and the variations in the electric field profile caused by non-uniform heating.

The electromagnetic field simulation was obtained by solving Maxwell's equations using a modal approach. The fields in the waveguide were formulated as a superposition of TE and TM modes. The effects of the coupling aperture, fiber, and short were included by applying boundary conditions on the transverse fields at the aperture and fiber interfaces. The aperture interaction was found by formulating a series dyadic Green's function for the magnetic surface current in the aperture. This was accomplished using mode-matching techniques. The method of moments was used to compute an approximate solution for the magnetic current, or aperture electric field, from which the unknown mode coefficients for the modal fields in the waveguide were found. To complete the solution, it was necessary to solve for the field interaction at the fiber interface to obtain the coefficients for the modes reflected from the fiber in terms of the coefficients for the modes incident on the fiber.

The field interaction with the fiber was developed using mode-matching techniques. This new approach provided a somewhat unique method for calculating the modal fields excited by the fiber for an incident set of modes. An equivalent electric surface current was used to model the fiber. The surface current was then approximated through a volume equivalence to relate the incident and reflected modes. The incident modes may be considered propagating or evanescent. For the experiment modeled in this analysis, all modes excluding the TE_{10} dominant mode were evanescent. Also, the effects

of the temperature-dependent permittivity of the fiber were contained in the analysis of the fiber.

4.2 Conclusion

In conclusion, electromagnetic field interactions with the aperture, fiber, and short caused slight variations in the electric field distribution in the cavity. The effects of shaping the aperture resulted in negligible variations in the electric field distribution at the fiber, a possible consideration for high-loss cavities. The y-component of the electric field evaluated at the fiber, which appears explicitly in the heat conduction equation, depends on the temperature dependent dielectric properties of the fiber and provides a method of coupling the electromagnetic and heat transfer solutions.

Simulations of the electric field distribution along the length of the cavity showed a slight peaking of the electric field at the fiber. This was consistent with known results for dielectric rods having electrically small diameters which place them in the Rayleigh scattering range. A shift in the resonant frequency of the cavity occurred for fibers of increasing diameter and permittivity.

The experiments performed at LANL and the corresponding heat transfer analysis by Goodson suggest that holding the amount of power absorbed constant led to an apparent control over thermal runaway. To maintain a constant level of absorbed power, it was found that the corresponding electric field has a large magnitude initially at low temperatures and decreases as the temperature of the load increases. The relationship between the computed electric field versus the dielectric loss of the load for a constant absorbed power exhibited the same trend as that predicted by a thermal approach.

Non-uniform heating effects were found to cause slight variations in the electric field profile along the axis of the fiber. An increase in the permittivity resulted in a decrease in the electric field strength along the fiber. This effect of the was demonstrated using two temperature distributions along the fiber. The fiber was approximated as an inhomogeneous material by sampling the variations in the typical permittivity along the fiber.

One advantage of the modal solution approach is that it provides a method of analyzing heating patterns in multi-mode cavities. Since the use of higher order modes is inherent in the development of the solution, they may be easily incorporated as propagating modes given the appropriate waveguide dimensions and frequency. A disadvantage of this approach is the limitation to a fiber or planar geometry. The approximations on the y-component of the electric field tangential to the fiber degenerate as the fiber diameter and relative permittivity increase. Therefore, the fiber must be thin relative to wavelength and the effective skin depth of the fiber. A more complete analysis could be accomplished with a finite discretization numerical method.

4.3 Recommendations

Future work is required to investigate the potential effects that the variations in the electric field profile have on the heat transfer solution by coupling to a heat transfer model. The temperature profile along the fiber for a given electric field profile would determine whether the change in the temperature due to the field variations is great enough to cause any further variations in the heat transfer solution. The finite-difference time-domain or finite-element methods could be implemented to give a more accurate analysis of the field interaction for thicker fibers and more importantly other ceramics having complex geometries. It is recommended that these approaches take into account the inhomogeneous nature of the material which results from the temperature-dependent dielectric properties. Multi-mode structures may also be of interest to investigate the possibility of obtaining a desired electric field distribution using higher-order, propagating modes.

References

[1] W. H. Sutton, "Microwave Processing of Ceramics - An Overview," *Microwave Processing of Materials III*, MRS Vol. 269, pp. 3-20, 1992.

[2] W. Duchez, "Role of Electric Field Profiles in Continuous Microwave Processing of Thermal Runaway Materials," M.S. thesis, Mechanical Engineering, Virginia Polytechnic Institute and State University, 1996.

[3] C. C. Goodson, "Simulation of Microwave Heating of Mullite Rods," M.S. thesis, Mechanical Engineering, Virginia Polytechnic Institute and State University, 1997.

[4] J. Tucker, R. Smith, M. F. Iskander, and O. M. Andrade, "Dynamic Model for Calculating Heating Patterns During Microwave Sintering," *Microwave Processing of Materials III*, MRS Vol. 269, pp. 61-67, 1992.

[5] V. M. Kenkre, "Theory of Microwave Interactions with Ceramic Materials," *Ceramic Transactions: Microwave Theory and Applications in Materials Processing II*, ACS Vol. 21, pp. 69-80, 1991.

[6] M. J. White, S. F. Dillon, M. F. Iskander, and H. D. Kimrey, "Finite-Difference Time-Domain Simulation of Microwave Sintering in a Variable-Frequency Multimode Cavity," *Microwave Processing of Materials V*, MRS Vol. 430, pp. 487-492, 1996.

[7] B. Chapman, M. F. Iskander, R. L. Smith, and O. M. Andrade, "Simulation of Sintering Experiments in Single-Mode Cavities," *Microwave Processing of Materials III*, MRS Vol. 269, pp. 53-59, 1992.

[8] D. C. Dibben, W. B. Fu, and R. Metaxas, "Numerical Models for the Sintering of Ceramics in a Multi-Mode Cavity," *Microwave Processing of Materials IV*, MRS Vol. 347, pp. 305-310, 1994.

[9] J. Clemens and C. Saltiel, "Numerical Simulation of Thermal Runaway in Alumina During Microwave Processing," Proceedings of the ASME Heat Transfer Division, HTD Vol. 317-2, pp. 381-389, 1995.

[10] J. R. Thomas, Jr., W. P. Unruh, and G. J. Vogt, "Mathematical Model of Thermal Spikes in Microwave Heating of Oxide Ceramic Fibers," *Microwave Processing of Materials IV*, MRS Vol. 347, pp. 363-368, 1994.

[11] G. A. Kriegsmann, "Cavity Effects and Hot Spot Formulation in Microwave Heated Ceramic Fibers," *Microwave Processing of Materials V*, MRS Vol. 430, pp. 181-186, 1996.

[12] C. V. Hile and G. A. Kriegsmann, "A Hybrid Numerical Method for Modeling Microwave Sintering Experiments," *Microwave Processing of Materials V*, MRS Vol. 430, pp. 319-324, 1996.

[13] G. J. Vogt, A. Regan, A. Rohlev, and M. Curtin, "Microwave Process Control Through a Traveling Wave Tube Source," *Microwave Processing of Materials V*, MRS Vol. 430, pp. 513-518, 1996.

[14] J. R. Thomas, Jr., C. C. Goodson, C. H. Stern, M. Jackson, and G. J. Vogt, "Microwave Sintering of Ceramic Rods: Experiments and Models," *The Journal of Microwave Power & Electromagnetic Energy*, Vol. 33, No. 2, pp. 113-120, 1998.

[15] C. A. Balanis, *Advanced Engineering Electromagnetics*, New York, John Wiley & Sons, Inc., pp. 25, 328, 1989.

[16] R. F. Harrington, *Time-Harmonic Electromagnetic Fields*, New York, McGraw-Hill, pp. 34, 71, 99, 129, 1961.

[17] R. E. Collin, *Field Theory of Guided Waves*, Piscataway, NJ, IEEE Press, pp. 184, 330-333, 1991.

[18] D. K. Cheng, Field and Wave Electromagnetics, Reading, MA, Addison-Wesley Publishing Company, pp. 559, 1992.

[19] M. Sadiku, *Numerical Techniques in Electromagnetics*, Boca Raton, FL, CRC Press, pp. 273-275, 1992.

[20] N. Marcuvitz, *Waveguide Handbook*, London, Peter Peregrinus Ltd., pp. 221-223, 266-267, 1986.

[21] W. H. Press, S. A. Teukolsky, W. T. Vetterling, and B. P. Flannery, *Numerical Recipes in FORTRAN: the art of scientific computing*, New York, Cambridge University Press, pp. 34-40, 1992.

[22] L. W. Couch, *Digital and Analog Communication Systems*, Upper Saddle River, NJ, Prentice Hall, pp. 105-108, 1993.

[23] J. E. Lanz, "A Numerical Model of Thermal Effects in a Microwave Irradiated Catalyst Bed," M.S. thesis, Mechanical Engineering, Virginia Polytechnic Institute and State University, 1998.

Vita

The author, Nathaniel D. Terril, was born in Wausau, Wisconsin on December 12, 1974 where he lived for five years. In 1980, his family moved to Herndon, a growing town in northern Virginia. He spent the next thirteen years in Herndon until he enrolled at Virginia Tech as an undergraduate in 1993. He earned his Bachelor of Science degree in electrical engineering in the spring of 1997. At this time he also began developing his skills as a graduate student under his advisor Dr. William A. Davis in the electromagnetics area. He received his Master of Science degree in Electrical Engineering in July 1998.